

The Magnetosphere-Ionosphere Observatory (MIO)

...a mission concept to answer the question “What Drives Auroral Arcs”

- ♥ Get inside the aurora in the magnetosphere
- ♥ Know you’re inside the aurora
- ♥ Measure critical gradients

writeup by: Joe Borovsky
Los Alamos National Laboratory
jborovsky@lanl.gov
(505)667-8368

updated April 4, 2002

Abstract: The MIO mission concept involves a tight swarm of satellites in geosynchronous orbit that are magnetically connected to a ground-based observatory, with a satellite-based electron beam establishing the precise connection to the ionosphere. The aspect of this mission that enables it to solve the outstanding auroral problem is “being in the right place at the right time – and knowing it”. Each of the many auroral-arc-generator mechanisms that have been hypothesized has a characteristic gradient in the magnetosphere as its fingerprint. The MIO mission is focused on (1) getting inside the auroral generator in the magnetosphere, (2) knowing you are inside, and (3) measuring critical gradients inside the generator. The decisive gradient measurements are performed in the magnetosphere with satellite separations of 100’s of km. The magnetic footpoint of the swarm is marked in the ionosphere with an electron gun firing into the loss cone from one satellite. The beamspot is detected from the ground optically and/or by HF radar, and ground-based auroral imagers and radar provide the auroral context of the satellite swarm. With the satellites in geosynchronous orbit, a single ground observatory can spot the beam image and monitor the aurora, with full-time conjunctions between the satellites and the aurora.

Table of Contents

<i>Section</i>	<i>Page</i>
1. Introduction and Synopsis	3
2. Why Study Auroral-Arc Generators?	5
3. The Mission Concept	8
3.A. Ascertaining the magnetic-field-line mapping	8
3.B Measuring gradients in the magnetosphere	19
3.C The Auroral Observatory	21
4. Other Science	25
4.A Magnetosphere-ionosphere coupling	26
4.B The cause of other types of aurora	27
4.C Quantifying the feedback of aurora on the magnetosphere	27
4.D Field-line mapping dynamics	28
5. Facility Use and Campaign Possibilities	29
6. EPO Themes	31
7. Summary	33
8. Personnel	34
Appendix A: Optical Spotting of the Illuminated Footpoint	35
Appendix B: Beam Divergence and the Loss Cone	41
Appendix C: Electrostatic Two-Stream Instabilities	59
References	62

1. Introduction and Synopsis

From the magnetospheric-physics point of view it can be said that the aurora is there for a reason, but we don't know why, and so we don't know the impact that the aurora has on the dynamics of the magnetosphere. From an auroral-physics point of view it can be said that no complete model of the aurora can be constructed because we don't know what is going on in the magnetosphere.

The aurora tap large amounts of energy from the Earth's magnetosphere, but we don't know what form of energy is tapped: be it $B^2/8\pi$ magnetic energy, $nk_B T_i$ ion thermal energy, $nk_B T_e$ electron thermal energy, $\rho \delta v^2$ turbulent flow energy, ρv^2 bulk flow energy, etc. With a large energy extraction, the aurora has an impact on the dynamics of the magnetosphere, but not knowing the form of the energy that is extracted, the nature of the impact is not known, be it morphological change, ion pressure release, electron pressure release turbulence dissipation, flow braking, etc.

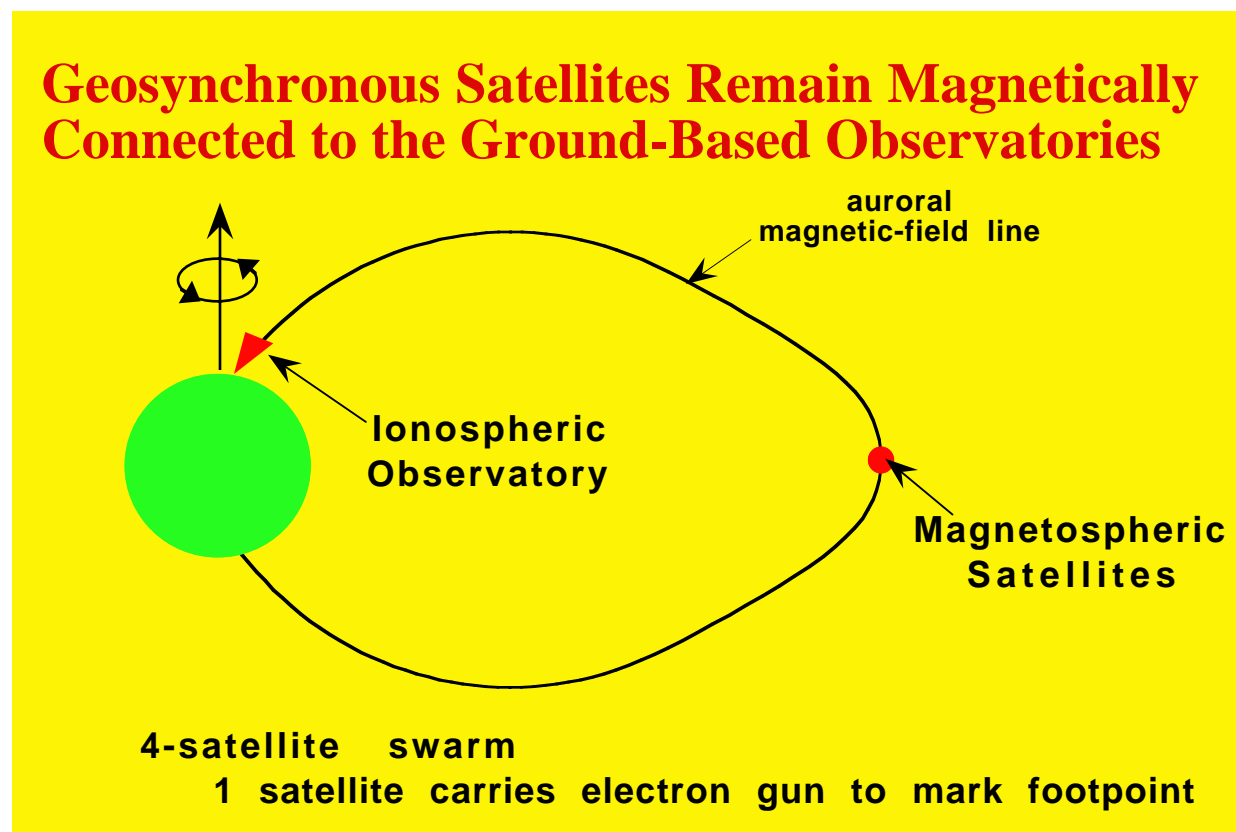


Figure 1. A sketch of an auroral-arc magnetic-field line with the locations of the MIO swarm of 4 satellites and the MIO ground-based auroral observatory shown.

To discern how energy is tapped from the magnetosphere, the Magnetosphere-Ionosphere Observatory (MIO) will determine the generator mechanism of discrete auroral arcs, which are the small-scale sites of large energy extraction. The strategy used by MIO to determine the mechanism that operates is (1) get tight cluster of satellites into the $\beta \sim 1$ magnetospheric end of an auroral arc, (2) unambiguously determine that the satellites are in the arc, and (3) measure critical gradients

across the arc. The critical step (2) is accomplished by means of an electron gun on one satellite in the swarm that fires a beam into the atmospheric loss cone to illuminate the ionospheric footpoint of the magnetospheric satellite swarm. Looking from the ground at the position of the marked footpoint in the context of the aurora, the times at which the satellite swarm crosses auroral arcs can be unambiguously determined.

The mission is comprised of 4 satellites in a tight swarm (~100-km separations) in the equatorial magnetosphere at geosynchronous orbit ($r = 6.6 R_E$) and a single ground-based observatory under the auroral ionosphere (see Figure 1). Spotting the illuminated magnetic footpoint will be done from the auroral observatory optically and/or via HF radar. Geosynchronous orbit is chosen because the footpoint will always be in view from a single ground station, providing full-time conjunction data between the satellite-swarm measurements in the magnetosphere and spatial-temporal images of the aurora in the ionosphere from the ground observatory.

2. Why Study Auroral-Arc Generators?

Auroral arcs are narrow east-west-aligned sheets of electron precipitation that produce east-west curtains of airglow in the upper atmosphere. The sheet electrons produce east-west channels of enhanced ionization in the ionosphere, and auroral arcs have intense field-aligned sheet currents. Auroral-arc magnetic-field lines are sites of intense energy extraction from the magnetosphere. This extracted energy goes into powering the electron sheet beams, which in turn deposit their energy in the upper atmosphere, and into the driving of current systems that close in the resistive ionosphere.

The aurora has a significant impact on the magnetosphere. About 30% of the energy budget of the magnetotail goes into Joule heating and precipitation heating of the auroral ionosphere. The impact of atmospheric precipitation losses in the auroral zone is also significant. About 10% of all plasma-sheet ions are lost to precipitation as the ions convect past the dipole from the nightside to the dayside and about 50% of all plasma-sheet electrons are lost to precipitation as they convect past the dipole from the nightside to the dayside.

The type of energy extracted by the aurora from the magnetosphere is not known, and so the impact of the aurora on the magnetosphere is not known. It has not been discerned whether $B^2/8\pi$ magnetic-field energy is extracted, or $nk_B T_i$ ion thermal energy, or $nk_B T_e$ electron thermal energy, or $\rho \delta v^2$ turbulent flow energy, or ρv^2 convective flow energy, etc. So it is not known whether the impact of auroral energy extraction is morphological change of the magnetosphere, ion pressure release, electron pressure release, turbulence dissipation, flow braking, etc. One cannot assess whether auroral energy extraction enables Earthward convection of the magnetotail (via morphology changes or pressure release reducing the entropy of flux tubes) or disables Earthward convection (via flow braking).

As noted in the sketch in Figure 2, an auroral arc involves two mechanisms, a generator mechanism that extracts energy from the magnetosphere to power the arc and an accelerator mechanism that produces the sheet beam of energetic electrons. The accelerator site plus the resistive ionosphere produce loads for the generator.

In Table 1 is a list of some of the generator mechanisms for auroral arcs that have been hypothesized in the literature (see *Borovsky* [1993] for elaboration of these mechanisms). Each mechanism has a unique magnetospheric fingerprint in the sense that it is associated with a unique radial gradient that can be measured in the magnetosphere. As noted in the table, the different auroral-arc-generator mechanisms have different consequences for the operation of the magnetosphere. One reason for wanting to determine which generator mechanism operates is that until the method of energy extraction is known, the effect that aurora have on magnetospheric dynamics cannot be ascertained and our understanding of magnetospheric evolution and dynamics will remain incomplete.

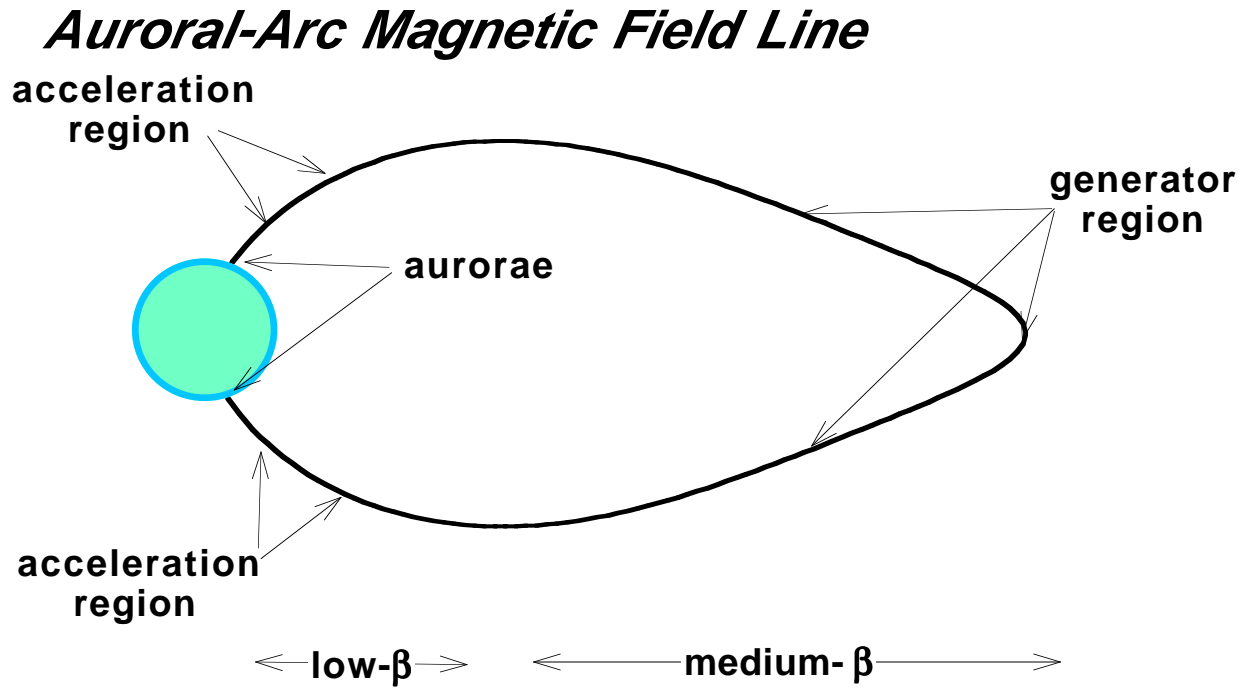


Figure 2. A sketch of an auroral-arc magnetic field line. Two mechanisms are operating, an accelerator mechanism is the very-low- β plasma near the Earth and a generator mechanism in the $\beta \sim 1$ magnetosphere.

Table 1. A list of hypothesized auroral-arc generator mechanisms, the gradient in the magnetosphere that will identify them, and their impact on magnetospheric dynamics should they operate.

<i>GENERATOR MECHANISM</i>	<i>UNIQUE OBSERVABLE</i>	<i>FEEDBACK ON MAGNETOSPHERE</i>
Velocity Shear	Abrupt velocity shift across arc	Auroral arcs act to brake magnetospheric flows
Ion Pressure Gradient	Ion-temperature jump across arc	Auroral arcs act to relieve pressure in the magnetosphere
Electron Pressure Gradient	Electron-temperature jump across arc	Auroral arcs act to Relieve Pressure in the magnetosphere
Resonance Absorption	Change in AC Poynting flux across arc	There is a rapid transport of energy to the plasma sheet
Particle Anisotropies	Change in pitch-angle distributions across arc	Auroral arcs act to cool the plasma sheet
Ionospheric-Conductivity Feedback	Distinct flow directions relative to arc drift	Ionosphere controls energy flow from the Magnetosphere
Ion Streams	Field-aligned ions within arc	Auroral arcs connect to particle-energization sites
Electrostatic Turbulence	Fluctuating E-Fields and flows around arc	Aurora dissipates flow turbulence in the magnetosphere
Plasma Flow across Conducting Channel	Deflection of radial flow across arc	Auroral arcs act to divert magnetospheric convection

Another reason for wanting to ascertain the generator mechanism of auroral arcs is that a

comprehensive model for an auroral arc is impossible to construct without knowing how the generator works. As depicted in Figure 2, an auroral arc involves an acceleration mechanism acting near the Earth and a generator mechanism acting out in the magnetosphere. Many space missions have been dedicated to studying the acceleration region of auroral arcs, e.g. INJUN-5, OGO-6, S3-3, DE-2, AUREOL-3, Viking, Akebono, Polar, Freja, Magion 2+3, Interball Auroral, and FAST, but no missions have been aimed into the generator region of auroral arcs. The science of the generator is overdue.

3. The Mission Concept

The MIO mission concept is 4 satellites in a tight swarm in the equatorial magnetosphere in geosynchronous orbit and a ground-based observatory under the magnetic footpoint of the swarm. One satellite carries an electron gun that is used to mark the magnetic footpoint of the swarm in the ionosphere. The ground-based observatory determines what kind of auroral features the satellite swarm is in and the swarm makes critical gradient measurements in the auroral magnetosphere. Auroral arcs are the primary focus of MIO.

The evidence that auroral arcs can be conjugate to equatorial magnetosphere at geosynchronous-orbit is threefold. The first evidence comes from the use of magnetic-field models to map low-altitude auroral structures outward along magnetic-field lines to the equatorial magnetosphere. For instance, the mapping of *Elphinstone et al.* [1991] finds that the auroral oval as seen by the Viking spacecraft can come deep into the dipolar magnetosphere on the nightside, e.g. in to $L \sim 5$. Similarly, *Lu et al.* [2000] find auroral intensifications mapping to the geosynchronous region of the magnetosphere. The second evidence comes from matching the electron distribution functions measured on low-altitude and equatorial spacecraft and then placing the low-altitude position of the best match into the context of the aurora from auroral images. For instance *Meng et al.* [1979] and *Mauk and Meng* [1991] found that auroral arcs could reside equatorward of the footpoint of a geosynchronous satellite in the equator, indicating arcs in the magnetosphere closer to the Earth than geosynchronous orbit.. The third evidence comes from the observations in the equatorial magnetosphere of outflowing auroral beams of electrons. For instance *McIlwain* [1975] and *Kremser et al.* [1988] saw beams of energetic, field-aligned electrons in the geosynchronous equator that are attributable to auroral-acceleration processes [e.g. *Boehm et al.*, 1995].

3.A. Ascertaining the magnetic-field-line mapping.

In the past, satellites have undoubtedly flown through auroral structures in the magnetosphere. Unfortunately, one can't tell when this occurred. Magnetic-field models of the magnetosphere are not accurate enough to be used to connect the positions of satellites in the magnetosphere to individual auroral features [*Hones et al.*, 1996; *Weiss et al.*, 1997]. Besides, auroral currents will produce localized distortions of the magnetic-field mappings that are not included in these field models. The only way to ascertain the magnetic-field-line connection between the magnetosphere and ionosphere accurately is with the use of an electron beam fired from the magnetosphere that illuminates the ionospheric footpoint of the field line.

By firing a beam of energetic electrons from a satellite into the loss cone, airglow and enhanced ionization can be produced in the upper atmosphere on the magnetic footpoint of the satellite. This airglow can be detected via a ground-based camera and/or this enhance ionization can be detected via ground-based HF radar. With either technology, the footpoint can be located and put into context with the aurora using auroral images obtained from the ground.

For optical detection to be feasible, the electron gun must be powerful enough so that the airglow of the beamspot in the ionosphere can be seen against an auroral-airglow background. A 10 kW beam will suffice (see Appendix A). For radar detection, the electron gun must produce a beam of sufficient power and sufficient total energy to create sufficient ionization in the upper atmosphere so that radar can produce a detectable echo. A 10-kW beam with a duration of 0.5 sec is more than sufficient (see Appendix B).

A beam-firing sequence of 0.5 seconds on, 0.5 seconds off, 0.5 seconds on is envisioned (see Appendix A). How often the beam is fired will be determined by the size of the solar panels on the gun-bearing satellite and by the choice of the power-storage system for the gun (batteries or capacitors). Firings of at least several times per hour are envisioned, with perhaps a burst mode controllable from the ground to use during optimal auroral times. The plasma contactor will be operated during the beam firings, so for a few-second-long interval during the operation of the electron gun and plasma contactor some of the measurements made by the gun-bearing satellite will be interfered with.

Owing to space-charge effects during the flight of the beam from the equator to the atmosphere, there is a limit to the number flux of electrons that can be shot into the loss cone. The concept of this limit is as follows (see Appendix C for elaboration). The beam of electrons is a long, cylindrical stick of negative space charge. The higher the current of the beam, the more electrons, and the greater the amount of space charge. The space charge of the beam produces a radial electric field which causes a radial expansion of the beam. The outward velocity of the beam electrons introduces a divergence angle to the beam, and since the beam is launched in the direction of the Earth's magnetic field, the divergence is synonymous with a spread in pitch angles. Too much space charge will result in too much radial expansion of the beam, which will result in too large a beam divergence to fit into the loss cone. Since the amount of space charge is proportional to the beam current, and because the power delivered by the beam is proportional to the beam current, a limit of the space charge represents limits on the power and current that can reach the atmosphere. The critical amount of space charge (which is a function of the beam velocity, the beam current, the initial radius of the beam, and the ambient magnetic field strength at the satellite), is calculated from numerical simulations of cylindrical electron beams. The simulations account for (a) the space-charge expansion of the beam, (b) the magnetic pinch force acting to oppose the expansion of the beam [Miller, 1982], (c) the Lorentz force of the radially expanding electrons moving across the Earth's magnetic field, and (d) the relativistic-mass effect which retards the expansion of the beam electrons. The dominant are (a) and (c). As the beam propagates it expands outward, with the expansion eventually being halted by the Lorentz force of the Earth's magnetic field. The limiting space charge (and power and current) is obtained by matching the angular divergence of the field-aligned beam to the size of the loss cone. The maximum power that can be put into the atmosphere from the geosynchronous equator is plotted as a function of electron-gun voltage in Figure 3. Details of the calculations appear in Appendix B.

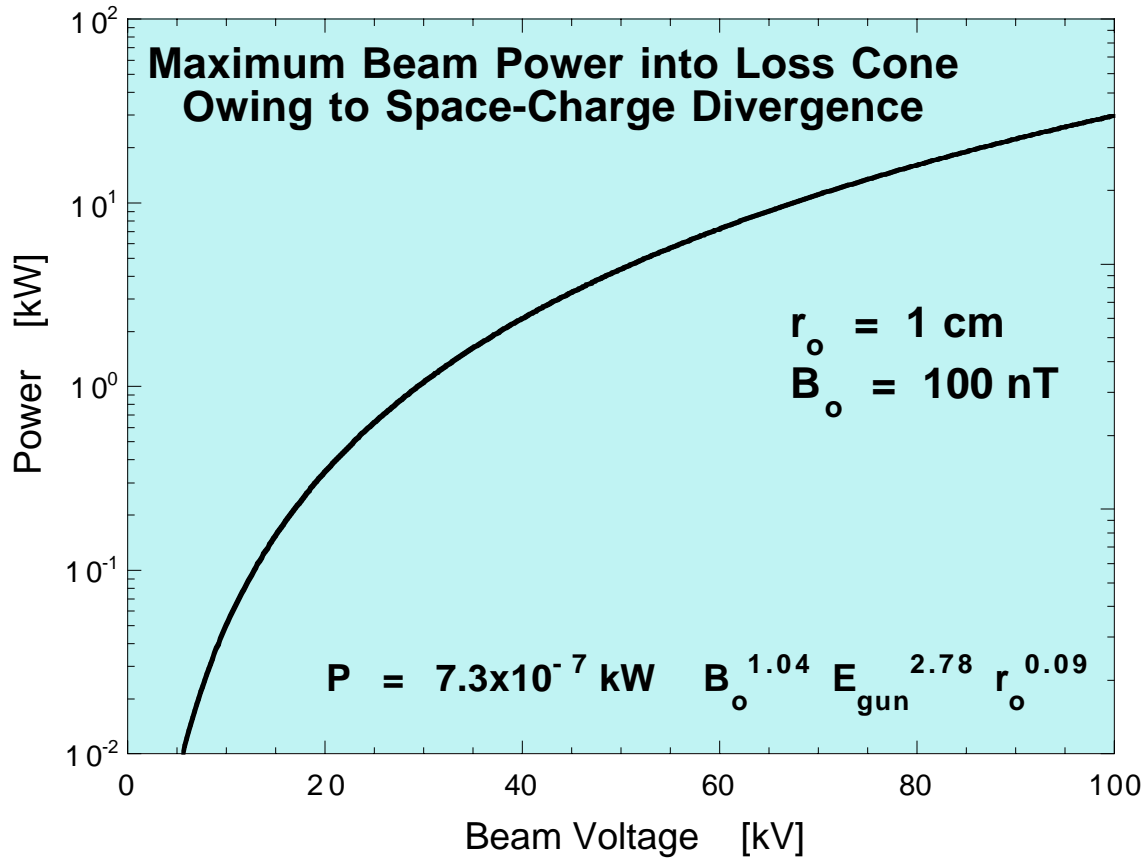


Figure 3. A plot of the maximum power that an electron beam can deliver to the atmosphere from the geosynchronous-orbit equator versus the beam voltage. The calculation is based on matching the amount of space-charge expansion of the electron beam after it leaves the electron gun with the angular size of the atmospheric loss cone. The empirical expression for the maximum power is shown in the figure.

There is a probability that ambient ions in the magnetosphere will react after about 10 msec to the space-charge electric field of the beam and will be drawn into the path of the beam to electrostatically shield the beam's space charge, which will reduce the divergence of the beam. This is known as "ion focusing" of the electron beam [Barov and Rosenzweig, 1994]. Should this ion focusing occur, it will be good: it will allow higher current beams to be used at lower gun voltages to deliver the power, which would save weight on the spacecraft. Since it is difficult to assess the effectiveness of this ion focusing, the MIO mission is designed without this ion focusing occurring.

The technology of operating high-power electron guns in space has been verified. Electron guns with powers of 30 kW [O'Neil *et al.*, 1978] and 40 kW [McNutt *et al.*, 1995] have been operated, beams with currents of up to 18 A have been flown [Rappaport *et al.*, 1993] and gun voltages of 45 kV [Winckler *et al.*, 1975] have been flown. Operating an electron gun in the low-density magnetosphere will require the use of a plasma contactor (see Table 3) that can emit an ion flux exceeding the electron-beam flux to prevent spacecraft charging during beam operations [Katz *et al.*, 1994; Prech *et al.*, 1995]. During the several-seconds-long interval of operation of the

contactor, some of the measurements on the gun-bearing satellite (e.g. electric fields) will be perturbed.

The 60-kV, 166 mA electron beam from the MIO electron gun should propagate through the magnetosphere without disruption by plasma instabilities. An assessment of the threat of plasma-wave instabilities driven by the electron beam propagating through the magnetospheric plasma found that electrostatic instabilities will not be a problem for beam propagation from the satellite to the atmosphere. The narrow, cylindrical beam makes a poor driver for plasma waves; hence the beam will not interact strongly with the magnetospheric plasma. Using the analysis of *Galvez and Borovsky* [1988], it is found that the absolute growthlength for streaming instabilities driven by the MIO beam is a few 10's of Earth radii for a continuous beam, and farther for a pulsed beam (see Appendix C for details). Hence, no scattering of the beam electrons is expected. For the MIO beam passing through the dense plasma emitted by the plasma contactor, Vlasov calculations [*Peter Gary*, private communication] find that the wavelengths of the plasma waves that the beam tends to drive are always much longer than the diameter of beam, so again, in the spirit of *Galvez and Borovsky* [1988], the beam cannot effectively drive an instability and the beam will not suffer scattering as it propagates through the dense plasma-contactor plasma. An assessment of the susceptibility of the beam to disruption by the hose or the sausage electromagnetic instabilities [*Miller*, 1982] found that neither instability will interfere with beam propagation through the magnetosphere. Experimentally, similar beams have been detected after long-distance propagation through the magnetosphere. Beams with energies of up to 40 kV were propagated long distances through the magnetosphere in the Echo series of experiments [*Hallinan et al.*, 1990; *Winckler*, 1992] and electron beams of 27 kV, 0.5 Amp and 15 kV, 0.5 Amp on the two ARAKS experiments were propagated 8.2 R_E through the magnetosphere without disruption [*Pellat and Sagdeev*, 1980; *Lavergnat*, 1992]

As discussed in section 3.B below, the optical beamspotting camera is envisioned to be a meso-scale CCD camera with a viewing angle of about 30° by 30° . The technology of optically detecting the illuminated footpoint has been verified: electron beams with less than 10 kW of power have been optically detected from the ground after they have propagated through the magnetosphere into the upper atmosphere. Two examples are the detection of a 3.4 kW beam by *Davis et al.* [1980] during the NASA 12.18 NE beam experiment using a ground-based image-orthicon television camera and the detection of a 2.4 kW beam in the Echo-4 experiment by *Hallinan et al.* [1990] using a ground-based image-orthicon television. In the Echo-4 experiment, the beamspot was imaged after the beam had propagated twice through the magnetosphere at $L = 6.5$.

The spatial distribution of the production of ionization in the upper atmosphere is calculated as follows. For a given beam power flux, beam radius, beam-electron energy, and beam-electron angular distribution at the top of the atmosphere, a large number of individual electrons that represent the distribution of beam electrons impinging on the atmosphere are followed computationally as they move through and interact with the atmosphere, precisely as was done in

the Appendix of *Borovsky et al.* [1991]. To follow the motion of the beam electrons in the atmosphere, the computer calculation iterates between three steps: the computer (1) solves the equations of motion for an electron in the Earth's magnetic field, (2) decreases the velocity of the electron according to a Bethe stopping-power equation for an electron in air, and (3) determines a probability for elastic scattering of the electron off air molecules as it moves and angular scatters the electron randomly according to that probability. The atmospheric profile is obtained from the MSIS-86 atmospheric model [*Hedin*, 1978], the stopping-power formulation is given by eq. 4-124 of *Marmier and Sheldon* [1969] with a mean ionization potential of 92 eV for nitrogen-like atoms [*Ahlen*, 1980], and the measured angular-scattering cross sections of *Riley et al.* [1975] and *Fink and Ingram* [1972] for electrons on nitrogen are used to construct elastic-scattering probabilities. The ionization produced by the electron along its path is calculated by assigned one ionization per 35 eV of energy lost [*Banks et al.*, 1974] on the path in step 2 above. The number of ionizations produced by the many electrons is binned onto a three-dimensional spatial grid with 2-m horizontal resolution and 1-km vertical resolution. The number of ionizations produced on the grid is converted to an ionization rate by comparing the number of electrons computationally followed to the actual number of beam electrons per second impinging on the top of the atmosphere.

The 60-kV MIO electron beam will produce an optical beamspot that is a cylinder with an effective height along the magnetic field of about 7 km and an effective width across the magnetic field of about 31 m (cf. Figure 4, 5, and 6). On the CCD image of the beamspotting camera, with a pixel resolution of about 0.5 km on the sky, the illuminated magnetic-field line will appear as a coherent streak aligned with the magnetic-field direction. The facts that the beam will form a multi-pixel streak and that subsequent beam-on and beam-off images will be compared, makes the detection of the MIO footpoint against an auroral-illumination background straightforward when there is 10 kW of beam power.

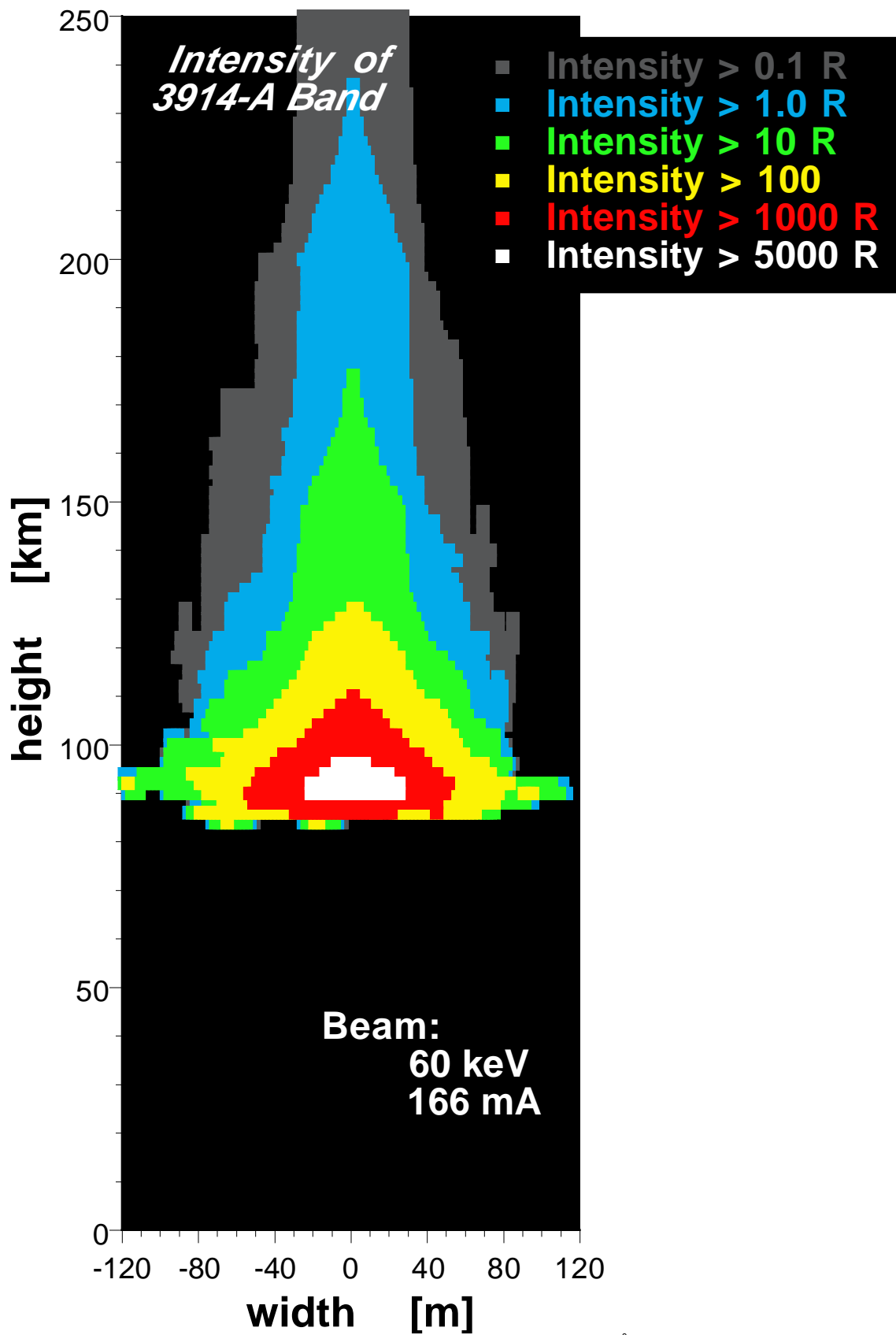


Figure 4. A computer calculation of the intensity of the 3914-Å band emission for a 60-keV, 166 mA beam of electrons hitting the upper atmosphere. The paths of 2000 beam electrons as they scattered through the upper atmosphere were followed. The Earth's magnetic field is taken to be vertical. The total amount of emission is 30 Watt.

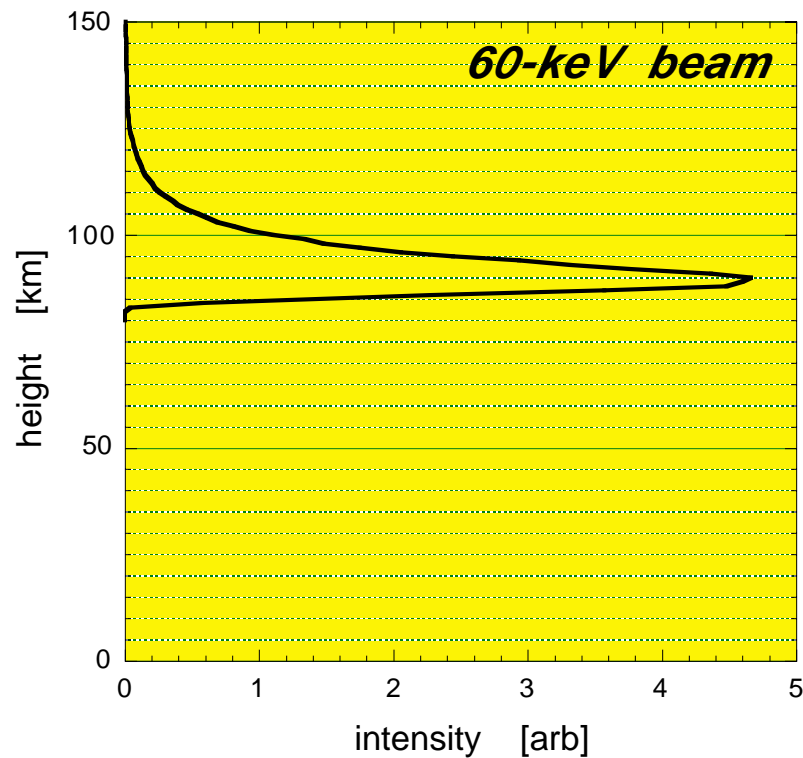


Figure 5. The vertical profile of airglow produced by 60-keV electron beams impinging on the topside of the ionosphere obtained by horizontally integrating the beamspot of Figure 4. The grid marks are 10-km apart.

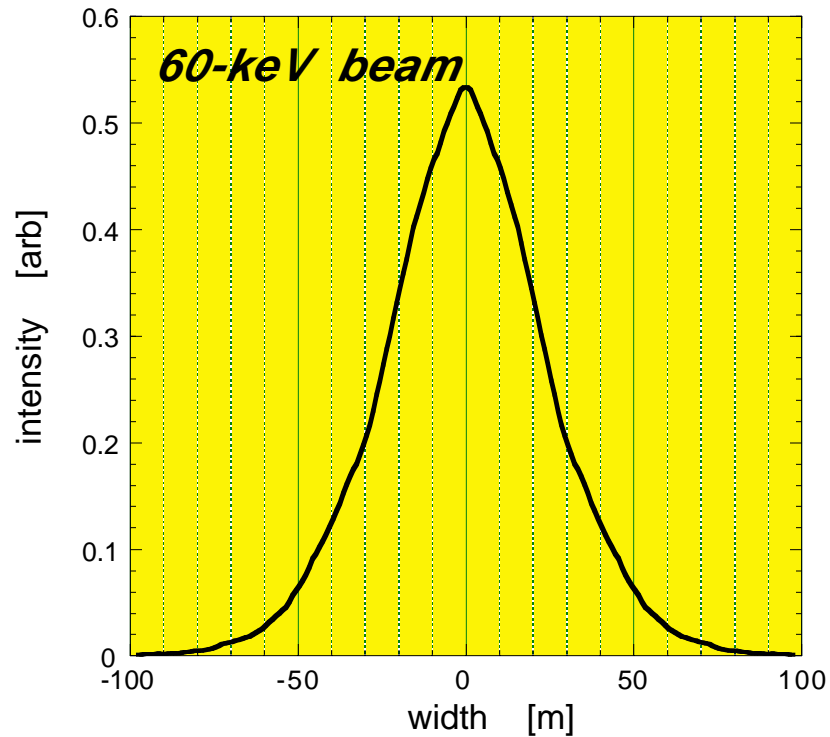


Figure 6. The horizontal profile of airglow produced by 60-keV electron beams impinging on the topside of the ionosphere obtained by vertically integrating the beamspot of Figure 4. The grid marks are 10-m apart.

Note that the beam of electrons will not exactly follow a single magnetic-field line from the gun satellite to the atmosphere. Owing to curvature and gradient drifts, the electrons of the beam will drift Eastward as they traverse the distance. In Figure 7 the total amount of eastward shift in the atmosphere is plotted as a function of the equatorial pitch angle of the beam electron. The loss cone is about 2.4θ . As can be seen, the shift in the beam entering the atmosphere is about 820 ± 15 meters eastward of the magnetic field line. For east-west aligned auroral structures this shift will not hinder determining such things as the times of auroral-arc crossings. This beam shift can be accounted for and the position of the footpoint can be determined to first order by subtracting the theoretical beamshift from the location of the sighted beamspot. As can be seen in Figure 7, in addition to the eastward shift, there is also an east-west spread to the beam entering the atmosphere. This spread is ± 15 m. (The gyroradius of a 60-keV electron normal to the magnetic field is 14 m.) This spreading is comparable to the spreading produced by atmospheric scattering (see Figures 4 and 6). In Figure 8 the north-south spread of the beam electrons as they enter the atmosphere is shown. As can be seen, the north-south spread is about ± 9 m. This is somewhat less than the spreading that will be produced by atmospheric scattering.

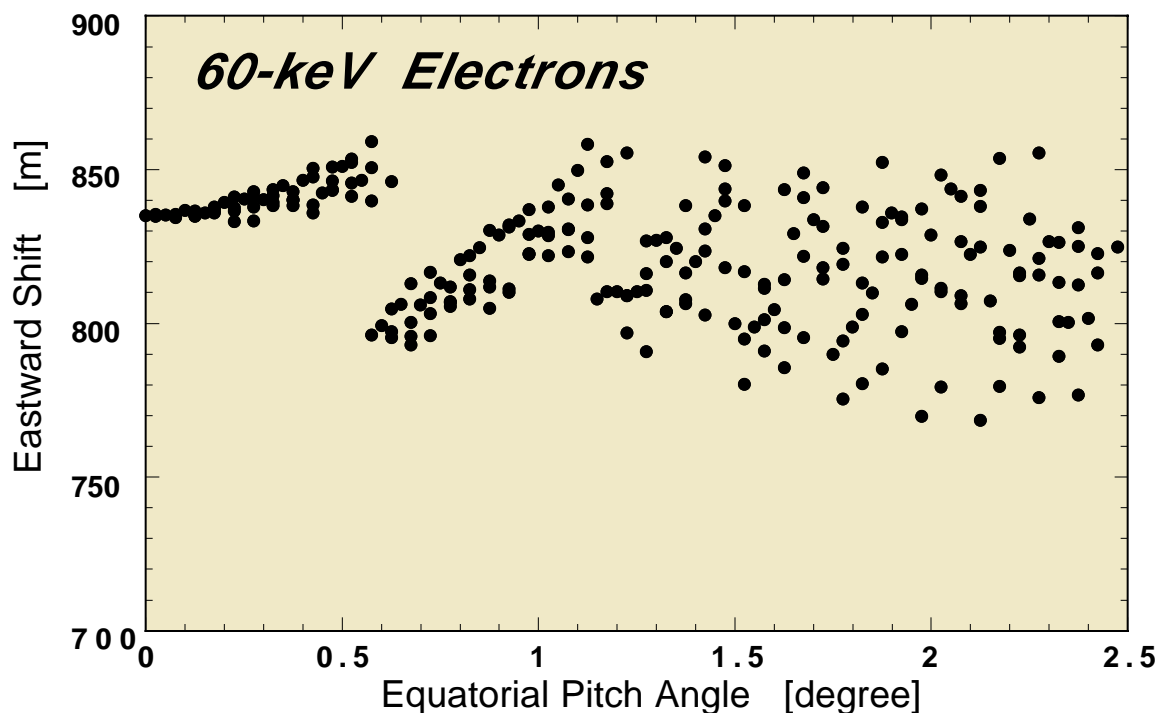


Figure 7. The eastward shift of the beam electrons in the atmosphere is plotted as a function of the equatorial pitch angle of the electron. The data is obtained from high-resolution electron-trajectory calculations in a dipole magnetic field.

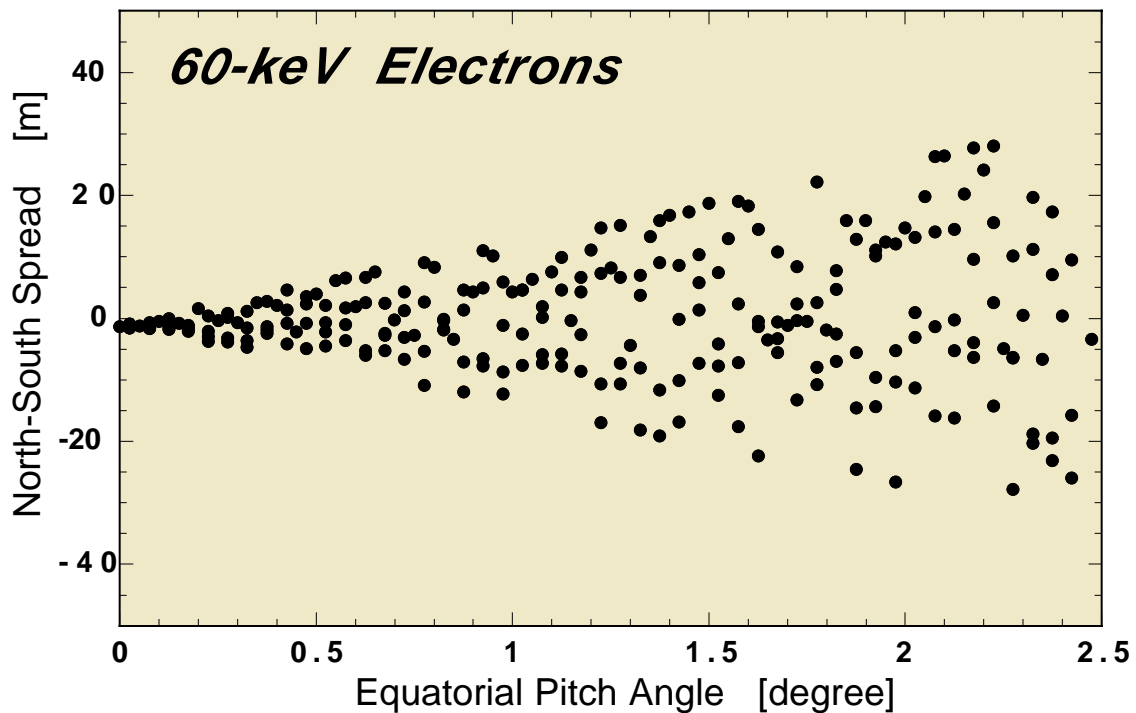


Figure 8. The north-south shift of the beam electrons in the atmosphere is plotted as a function of the equatorial pitch angle of the electron. The data is obtained from high-resolution electron-trajectory calculations in a dipole magnetic field.

Ground-based radars can also detect the enhanced ionization of the beamspot. The signal is extremely strong if the electron plasma frequency of the enhanced ionization region is above the frequency of the radar. In that case the beamspot is overdense and there is total reflection of the radar waves off the beamspot. If the electron plasma frequency of the enhanced ionization of the beamspot is less than the radar frequency, there is partial reflection of the radar waves off of the column of enhanced ionization. Calculations of the density of ionization produced by electron beams similar to that of MIO [Ray Greenwald and Jan Sojka, private communication] find that overdense regions will be produced, yielding extremely robust radar-backscatter signals. The technology of detecting the footpoint with radar has been verified: VHF-radar detection of beamspots after passage through the magnetosphere into the atmosphere have been made for the 3-kW beams of the Zarnitza-2 experiment [Zhulin *et al.*, 1980] and 40-MHz-radar detection of beamspots after passage through the magnetosphere into the atmosphere have been made for the 14-kW beams of the two ARAKS experiments [Uspensky *et al.*, 1980; Izhovkina *et al.*, 1980].

MIO Footpoint Location

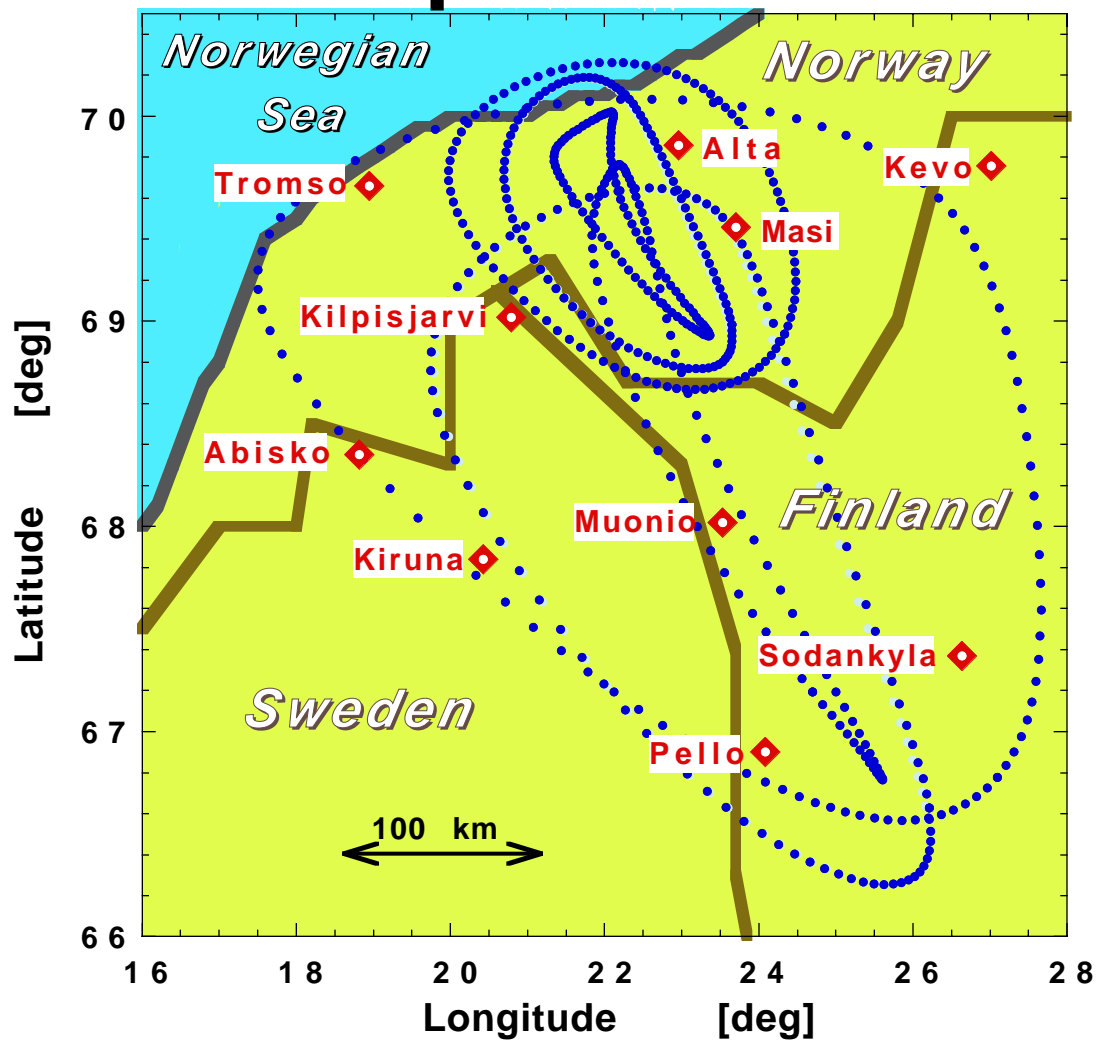


Figure 9. For an example longitude that puts the MIO footpoint in Northern Scandinavia, the approximate position of the footpoint of the MIO gun satellite in the ionosphere is plotted (blue) for 8 cases: Spring, Summer, Winter, and Fall for $K_p=0$ and $K_p=4$. Each case shown is 24 hours of footpoint position. The footpoints were obtained using the Tsyganenko T89 and the IGRF magnetic-field models.

MIO Footpoints on the Sky

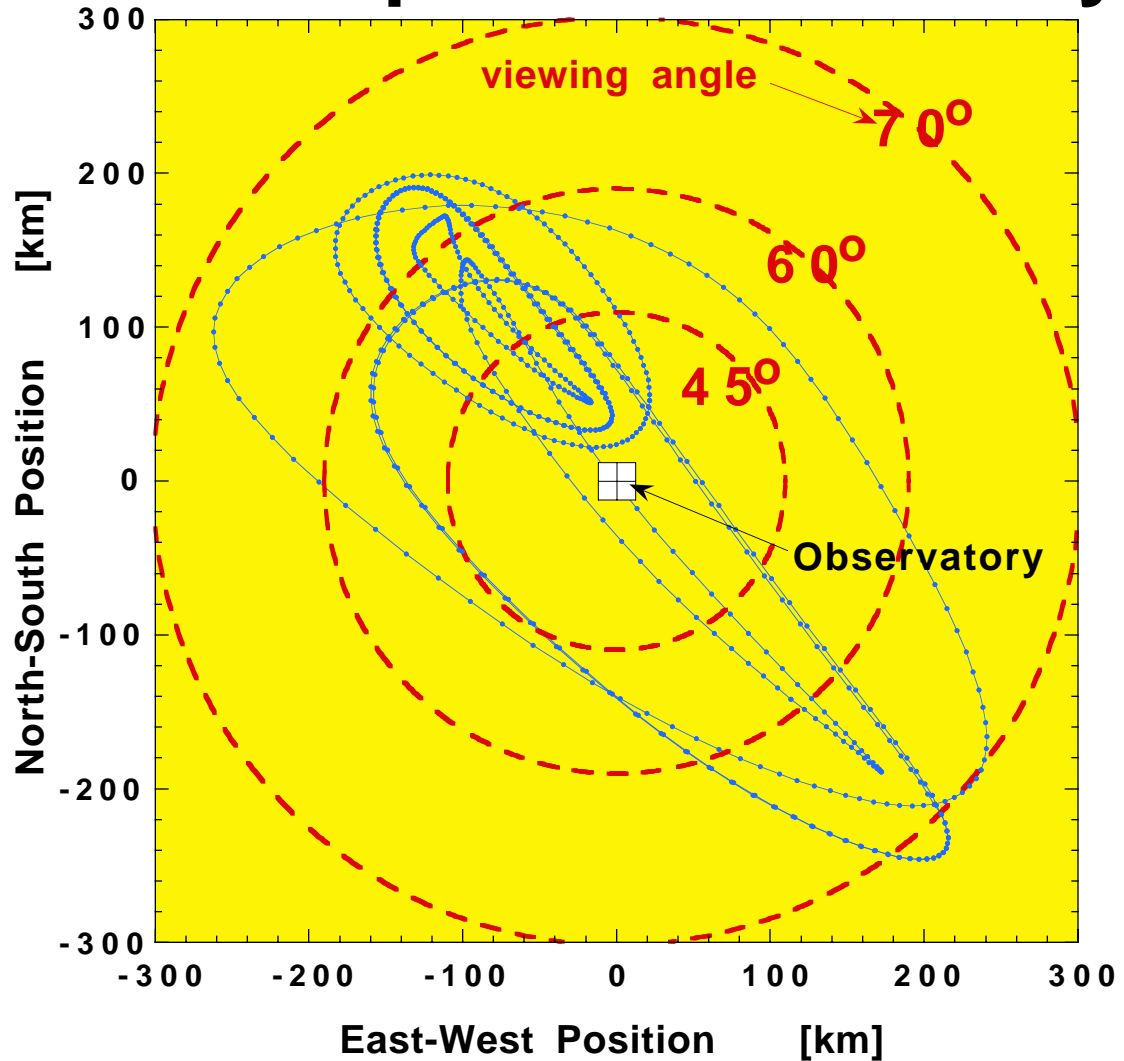


Figure 10. The approximate position of the footpoint of the MIO gun satellite in the ionosphere is plotted (blue) for 8 cases: Spring, Summer, Winter, and Fall for $K_p=0$ and $K_p=4$. Each case shown is 24 hours of footpoint position. The footpoints were obtained using the Tsyganenko T89 and the IGRF magnetic-field models. Shown as the circles (red) are the zenith viewing angles for the auroral observatory in the center of the plot.

By choosing geosynchronous orbit for MIO, the magnetic footpoint of the satellite swarm can be viewed from a single ground site. An estimate of the diurnal path that the footpoint of a geosynchronous satellite makes in the atmosphere can be seen in Figures 9 and 10. In each figure, eight hypothetical diurnal paths are shown in the figure: low- K_p and high- K_p for Winter, Summer, Spring, and Fall. The longitude of the MIO swarm is taken in this example such that the footpoint site is in northern Scandinavia. The footpoint estimates are obtained by tracing field lines from the geosynchronous equator to the atmosphere in the Tsyganenko T89 [Tsyganenko, 1989] magnetic field model, combined with the IGRF model. Note that tests show that the geosynchronous mapping of these models can be in error by several degrees of latitude (several hundred km) in the

ionosphere [e.g. Weiss *et al.*, 1997]. The actual diurnal path of the footpoint will ramble in the vicinity of the hypothetical paths as geomagnetic conditions varies throughout the day. Depicted Figure 10 (red circles) are the zenith-observing angles of the ionosphere at auroral heights as seen from a ground observatory at the center of map.

3.B Measuring gradients in the magnetosphere.

East-west-aligned auroral arcs correspond to azimuthally aligned structures in the geosynchronous-orbit equatorial magnetosphere. For a dipole field (which is approximately the case at geosynchronous orbit under normal geomagnetic-activity levels), the geometric north-south compression factor owing to the convergence of magnetic-field lines is about 33:1. Hence, an arc structure that is 1-km thick in the north-south direction in the ionosphere magnetically maps to a structure that is 33-km thick in the radial direction in the equatorial magnetosphere. (As a note, the east-west/azimuthal compression factor is about 17:1.) Thicknesses of a few km in the ionosphere are the most interesting for auroral-arc science. Hence, satellite separations of 100 km or so in the geosynchronous equator are most appropriate.

In Figure 11, the orbits of 4 geosynchronous satellites are sketched. Each orbit is nearly circular and has a period of 24 hours. Snapshots of the satellite positions are shown every three hours in the figure. Three satellite orbits are in the equatorial plane and a fourth is tilted out of the plane. Noting the 3 orbits in the plane, the satellites perform a daily dance around each other. Throughout the dance, the ability to measure radial and azimuthal gradients with the swarm of three is maintained. The fourth satellite rocks above and below the equatorial plane once per day, yielding the ability to measure poloidal (along the magnetic field) gradients at most times.

Daily Evolution of the 4-Satellite Configuration

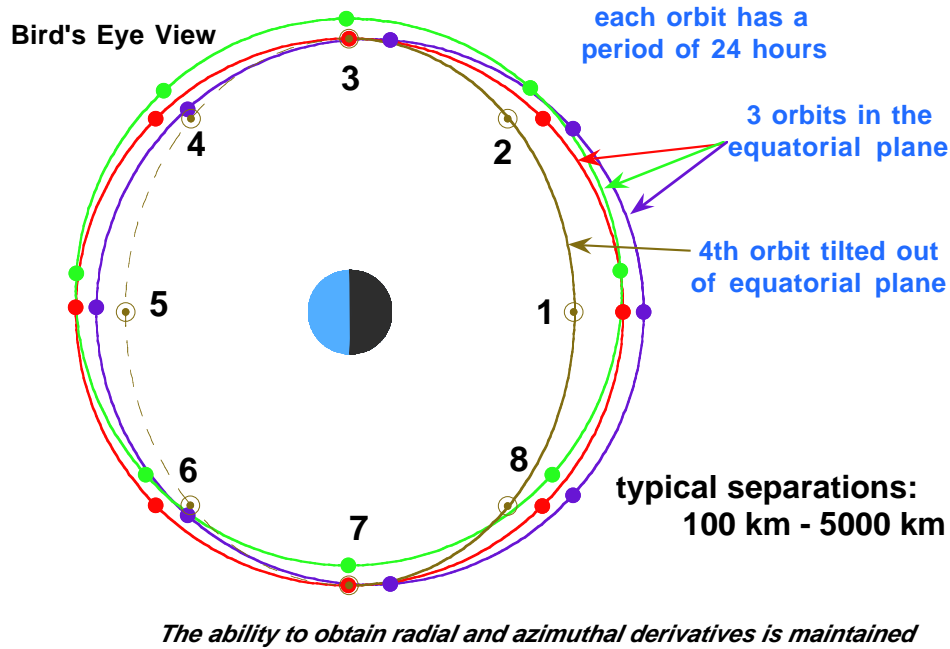


Figure 11. The diurnal dance of the 4 MIO satellites, shown every three hours. All orbits are nearly circular with periods of exactly 24-hours. The satellite separations are shown larger than the actual case. The radii of the orbits will be $6.6 R_E$, which is about 36,000 km, and the separations between satellites will be about 100 km.

Table 2. Typical parameters of the electron-plasma-sheet plasma at geosynchronous orbit on the nightside. The electron plasma sheet is the magnetospheric home of the aurora.

PARAMETER	EXPRESSION	VALUE
hot-plasma density	n	0.75 cm^{-3}
ion temperature	T_i	12 keV
electron temperature	T_e	1.5 keV
cold-ion density	n_{cold}	$< 10^{-2} \text{ cm}^{-3}$
magnetic field strength	B	100 nT
plasma beta	β	0.4
ion inertial length	c/ω_{pi}	260 km
ion gyroradius	r_{gi}	110 km
electron skin depth	c/ω_{pe}	6 km
electron gyroradius	r_{ge}	0.9 km
Debye length	λ_{De}	0.3 km

In Table 2, typical plasma parameters for the geosynchronous-orbit nightside

magnetosphere are listed. Note that with satellite separations of ~ 100 km, structures smaller than the ion inertial length c/ω_{pi} are being looked at. That is, the structures being measured in the magnetosphere are smaller than MHD structures.

The primary objective of MIO is to determine how the magnetosphere drives auroral arcs. The critical gradients to measure are listed in Table 1. To measure these gradients the satellites all must be instrumented with (see Table 3) electric-field instruments to accurately measure the plasma flow, ion instruments to measure the ion temperature and density and the 3-dimensional ion distribution function, electron instruments to measure the electron temperature and density and the 3-dimensional electron distribution function, and magnetometers to measure the direction and magnitude of the magnetic field. Instrument time resolutions of about 1 second are necessary, based on a 1-km-thick arc drifting at less than 1 km/s in the ionosphere.

Table 3. A list of the instruments on the satellites in geosynchronous orbit.

<i>INSTRUMENT</i>	<i>NUMBER OF SATELLITES</i>	<i>PRIMARY OR SECONDARY SCIENCE</i>
electric field	all	primary
plasma ions	all	primary
plasma electrons	all	primary
magnetic field	all	primary
electron gun	1	primary
plasma contactor	1	primary
ion composition	1	secondary
loss-cone particle resolution	1	secondary
waves	1	secondary
energetic particles	1	secondary

3.C The Auroral Observatory.

Locating the satellite swarm in the geosynchronous equator $L = 6.6$, which maps to magnetic latitude $\Lambda = 67^\circ$ in the ionosphere, has several advantages. (1) The satellites and the ground observatory stay magnetically linked together as the Earth rotates. This means that a lot of conjunction data between multipoint measurements in the magnetosphere and spatial-temporal images of the aurora in the ionosphere will be obtained. (2) The satellite footprints are always in view of a single ground station. This simplifies optically locating the beamspot and simplifies the coordination of auroral images with the beamspot location. (3) The auroral structures pass over the satellites rather than the satellites making rapid flythroughs of the auroral structures. This lessens the time-resolution requirements of the satellite instruments and also means that the time evolution of the aurora can be diagnosed. (4) Telemetry and orbital dynamics are straightforward. The satellite swarm can be continuously telemetered from a single ground receiver, and in fact the receiving groundstation can be co-located with the auroral observatory. (5) The geosynchronous magnetosphere/auroral ionosphere is rich in phenomena. This last point will be discussed in section 4.

In Table 4 the instrumentation required for the single ground-based auroral observatory is

listed. The fundamental instruments to accomplish the primary science are an optical beam-spotting camera and an optical all-sky camera.

Table 4. A list of the instrumentation at the single ground-based auroral observatory.

<i>INSTRUMENT</i>	<i>PRIMARY OR SECONDARY SCIENCE</i>
optical beam-spot locator	primary
all-sky camera	primary
radar	backup to primary
scanning photometer	secondary
magnetometer network	secondary
ionosonde	secondary
ionospheric heater	secondary
wave transmitter	secondary
telescope	secondary
balloon-borne x-rays	secondary
DMSP precipitating particles	secondary

The optical beam spotter is envisioned to be a CCD camera with a field of view that is on the order of 30° by 30° . Camera would be filtered on a prompt molecular band such as 3914-Å of 4278-Å. With a 256-by-256 pixel CCD, resolution on the sky of about 0.5 km will be obtained. With a temporal pattern of electron-gun firing such as beam on, beam off, beam on, beam off, a series images of the vicinity of the sky where the beamspot is expected will be taken, timed with the satellite beam-firing sequence plus a ~ 0.35 -second delay to account for beam propagation from the geosynchronous equator to the ionosphere. Consecutive beam-on and beam-off images will be differenced to look for the beamspot. With a 10-kW beam, beam-on and beam-off intervals with durations of about 0.5 second are envisioned to produce sufficient photon statistics to discern the beamspot from an auroral-airglow background without having too much temporal change in the aurora itself from image to image (see Appendix A). In addition to locating the beam spot, this camera would be used to put the beamspot into the context of auroral structures.

As shown in Figure 10, a single ground station can view the magnetic footpoint of the geosynchronous swarm of satellites. In the figure, estimates of the diurnal motion of the footpoint of a single satellite is shown for eight cases: low-Kp and high-Kp for Spring equinox, Summer solstice, Fall equinox, and Winter solstice. A longitude putting the footpoints in the Northern Scandinavia region was chosen and field lines were traced from the geosynchronous equator to the upper atmosphere using the Tsyganenko T89 and IGRF magnetic field models. Once the location of the magnetic footpoint of the gun satellite is experimentally determined, the locations of the footpoints of the other satellites in the swarm will be calculated from knowledge of their magnetospheric positions using a magnetic-field model to propagate the inter-satellite spacings along the magnetic field to the atmosphere. Some thinking will go into building such a local-B model, which will probably use information about the experimental mapping of the gun and information about the magnetic field measured on the satellites to fit a perturbed dipole/IGRF model so that the model is locally correct in its mapping.

The optical-all sky camera would probably be an intensified television camera or CCD camera. Taking sequential images through a series of filters (e.g. white light, 3914-Å or 4278- Å, 5577- Å, and 4861- Å) will provide information about electron and proton precipitation regions and crude information about the energy of the precipitating electrons. At the observatory site, a single wide-angle camera or a battery of medium-angle cameras could be used. To reduce the severity of the slant-angle viewing of aurora that is not overhead, outlying all-sky camera sites would be helpful: perhaps one site ~200 km to the north of the observatory and another ~200 km to the south. The all-sky images of the aurora will be used to give context to the meso-scale images of the aurora obtained with the beam spotter CCD camera.

As an adjunct to locating the beam spot optically, HF radar that covers the ionosphere above the ground observatory could also be used. Radars can put the MIO footpoint into the context of auroral flow patterns and radars also enable MIO studies to be made that connect phenomena in the dayside magnetosphere to the dayside ionosphere. Radar is discussed further in section 3.A.

Other ground-based instruments are useful to enhance the science of MIO (see Table 4, section 4, and section 5). Wavelength-filtered scanning photometers and magnetometer chains could be used to put the satellite footpoints into the context of proton aurora and Birkeland current systems, respectively. Ionosondes would be useful to establish correlations between ionospheric parameters and magnetospheric parameters. Ionospheric heaters focused on the satellite footpoint would be useful for conducting experiments in magnetosphere-ionosphere coupling and ground-based wave transmitters operating under the satellites footpoint would be useful for conducting experiments on the transmission of waves through the ionosphere and the propagation of waves in the magnetosphere (see section 5). Ground-based auroral telescopes pointed into their magnetic zeniths would be useful for studying the fine-scale structure of discrete auroras and correlating these structures with phenomena in the magnetosphere. Balloon-borne x-ray imagers and conjunctions with DMSP-satellite measurements of particle precipitation would be useful for correlating magnetospheric-generator conditions with the conditions of the auroral-electron accelerator above the atmosphere (see section 5).

In Figure 12, the Northern-Hemisphere location of the magnetic footpoint of geosynchronous-orbit magnetic-field lines are shown, the high-latitude curve being the local-noon positions of geosynchronous-orbit at all longitudes and the lower-latitude curve being the local-midnight positions for high-Kp of the geosynchronous-orbit footpoints for all longitudes. Some longitudes, such as central Alaska or northern Scandinavia are advantageous for locating the ground observatory over others. In particular, Scandinavia is extremely well instrumented with networks of all-sky cameras, high-resolution ionospheric radars, ionospheric heaters, magnetometer chains, and more.

Geostationary Northern Footprint for all longitudes
 at local noon and local midnight
 For date: 19950321
 IGRF Internal, T89 external model
 $K_p = 4$

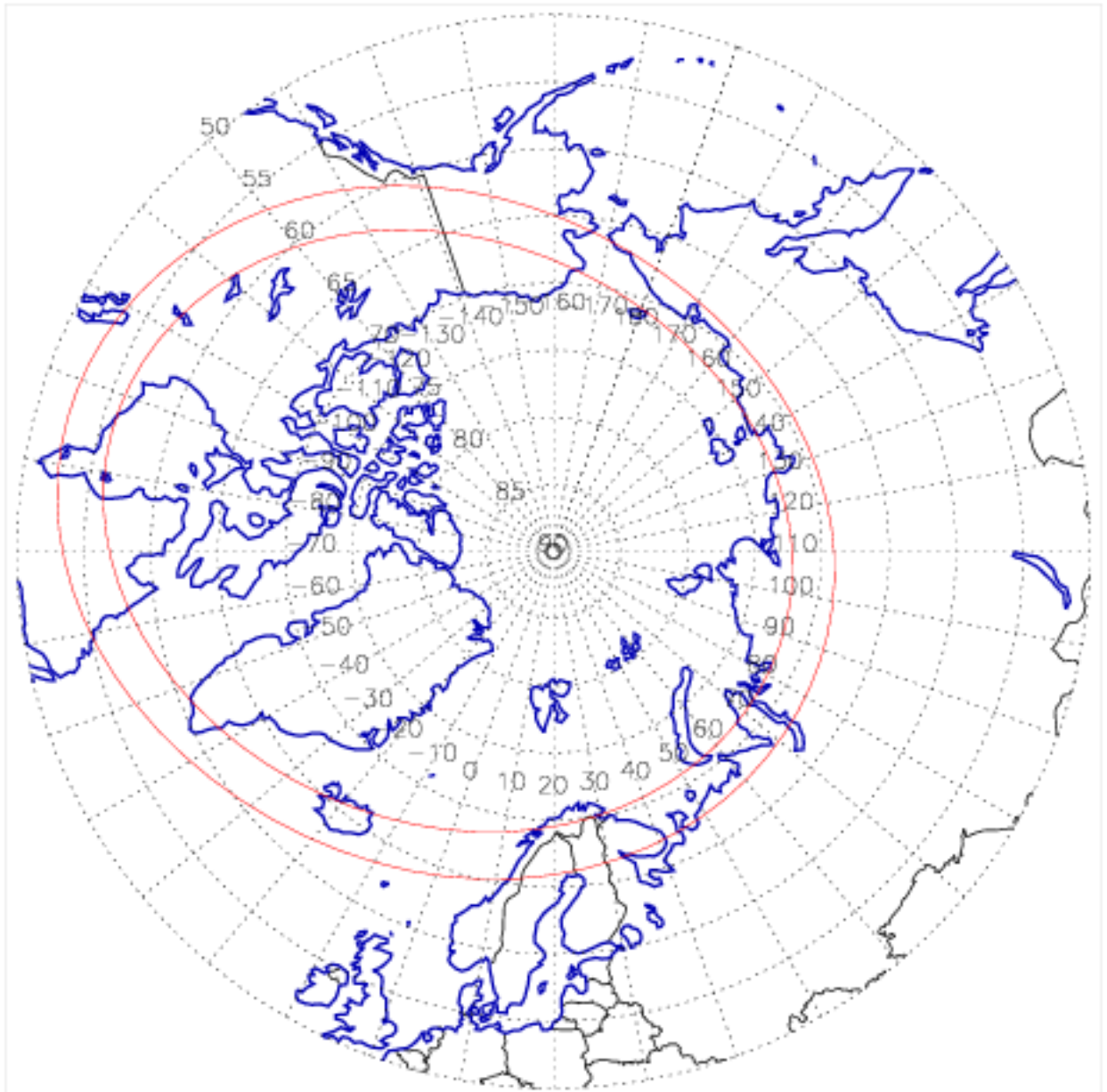


Figure 12. An indication of where geosynchronous footpoints lie geographically. The upper red curve is the location of magnetic footpoints connecting the geosynchronous-orbit equator to the ionosphere for local noon $K_p=4$ and the lower red curve is the footpoints for local midnight $K_p=4$. The footpoint locations were obtained with the Tsyganenko T89 and IGRF magnetic-field models (courtesy of Reiner Friedel).

4. Other Science

The geosynchronous magnetosphere ($L=6.6$) and its conjugate auroral ionosphere (invariant latitude $\Lambda=67^\circ$) are rich in phenomena. In Table 5 the regions of the magnetosphere that are seen by a satellite in an equatorial geosynchronous orbit are listed, along with the typical local times that those regions are seen each day. The electron plasma sheet is where one finds auroral arcs, but other phenomena are found in other regions. Among the phenomena seen in the geosynchronous equator are aurora, substorm injections, substorm stretching and dipolarization, Pc oscillations, plasmaspheric drainage plumes, ionospheric ion outflows, and atmospheric-source-cone electron beams. Among the phenomena seen in the $\Lambda=67^\circ$ conjugate ionosphere are aurora (arcs, diffuse, proton, black, patches, etc.), electrojets, ionospheric outflows, the mid-latitude trough, subauroral ion drifts (SAIDs), and F-region ionization patches.

Table 5. Regions of the magnetosphere that are seen by satellites with equatorial geosynchronous orbits. The local times at which those regions are seen are noted for typical days and for unusual days, where unusual can be extremely quiet or extremely active times.

<i>REGION SEEN AT GEOSYNCHRONOUS</i>	<i>LOCAL TIMES (TYPICAL)</i>	<i>LOCAL TIMES (UNUSUAL)</i>
ion plasma sheet/partial ring current	all	all
electron plasma sheet	nightside	none
electron trough	dayside	dayside
outer radiation belt	all	all
plasmasphere	dusk	all
magnetosheath	none	dayside

In addition to the aurora-arc generator, the MIO mission will prove to be a unique facility for studying (A) magnetosphere-ionosphere coupling, (B) the causes of other types of aurora, (C) the feedback of the aurora on the magnetosphere, and (D) field-line-mapping dynamics. Various aspects of those four topics are described in the four subsections below. Some studies may require changing satellite separations (see Table 6) in the magnetosphere, some may require secondary instrumentation on one satellite (see Table 3) and/or at the ground observatory (see Table 4).

Table 6. For various phenomena that MIO can investigate, the direction of the gradient to measure and the necessary satellite separations at geosynchronous orbit are listed.

<i>PHENOMENON INVESTIGATED</i>	<i>GRADIENT TO MEASURE</i>	<i>SATELLITE SEPARATION</i>
<i>Primary Science Objective</i>		
Auroral-arc generator	radial	~100 km
<i>Secondary Science Objectives</i>		
Launching Alfven waves	out of plane	1000-5000 km
Driving field-aligned currents	radial	various
Driving Region-II currents	radial	~5000 km
Structure of field-line resonances	radial	1000 – 5000 km
Convection E-field shielding	radial	~5000 km
M-I flow slippage	single satellite	0
Driving of ionospheric outflows	single satellite	0
Sub-auroral ion drifts (SAIDs)	radial	1000-5000 km
Diffuse aurora driving	single satellite	0
Proton aurora driving	single satellite	0
Cause of pulsating aurora	single satellite	0
Mapping to auroral patches	radial + azimuthal	~500 km
Cause of black aurora	radial	~100 km
Dynamics of M-I connectivity	single satellite	0
Magnetic shear across arcs	radial	~500 km

4.A Magnetosphere-ionosphere coupling.

With its ability to unambiguously determine the ionospheric location of the magnetospheric satellite's magnetic footpoint and thus to coordinate magnetospheric and ionospheric measurements, MIO provides a unique facility to study magnetosphere-ionosphere coupling. An extensive list of magnetosphere-ionosphere-coupling questions that can be addressed with MIO can be generated.

With its multiple satellites in the magnetosphere and with ground-based magnetometer chains providing information about currents in the ionosphere (see Table 4), MIO can discern how the magnetosphere drives field-aligned current systems that close in the ionosphere. With the use of the fourth (out of equatorial plane) satellite (see Figure 10), MIO can investigate Alfven-wave propagation and can discern what in the magnetosphere launches Alfven waves in the auroral arc current system. By measuring flows in the ionosphere with radar and comparing with flow

measurements in the conjugate magnetosphere, the question of who leads convection in the auroral zone – the ionosphere or the magnetosphere – can be answered, with implications as to who drives whom convection wise. Ionospheric particle outflows into the magnetosphere as seen on the equatorial satellites, can be correlated with auroral images, ionospheric flows, and magnetospheric conditions to investigate what kind of aurora lead to outflows and to the connection of outflows with frictional heating. The connection between auroral motions and magnetospheric flows are also straightforward to investigate. With wide satellite separations, the mechanisms acting in the magnetosphere to shield the convection electric field (e.g. Alfvén layers, the plasmapause,) can be discerned. Other questions such as “what in the magnetosphere drives subauroral ion drifts (SAIDs) in the ionosphere?”, “what is the radial structure of a field-line resonance?”, and “do auroral-arc equipotential structures extend to the equator?” can be answered using MIO.

4.B The cause of other types of aurora.

With MIO, examining the various magnetospheric conditions when the satellite footprint is in the various types of aurora is straightforward. These types are listed in Table 7, along with outstanding issues associated with the causes of these aurora. The issues listed can all be addressed by MIO, although secondary instrumentation on one satellite may be required (see Table 3).

Table 7. Outstanding issues that MIO will address that are associated with the causes of the various types of aurora.

<i>TYPE</i>	<i>OUTSTANDING ISSUES THAT MIO WILL ADDRESS</i>
Diffuse aurora	What is the source of electron pitch-angle scattering?
“ ”	What controls the size of the electrostatic loss cone?
Proton aurora	What is the cause of the proton pitch-angle scattering?
“ ”	What controls the proton pitch-angle scattering?
Pulsating aurora	What modulates the pitch-angle-scattering rate?
“ ”	What modulates the size of the electrostatic loss cone?
“ ”	What else goes on in the magnetosphere?
Drifting patches	What magnetospheric features map to the patches?
“ ”	What in the magnetosphere matches the velocity of the patches?
Black aurora	What causes the occurrence of black aurora?
“ ”	What magnetospheric features map to black aurora?

4.C Quantifying the feedback of aurora on the magnetosphere.

The several types of aurora can have differing effects on the magnetosphere. In Table 1, the differing manners of feedback on the magnetosphere of auroral arcs for the differing generator mechanisms that may operate were listed. To discern the feedback of the aurora on the

magnetosphere, the time evolution of the magnetospheric plasmas will be examined in conjunction with the various types of auroral activity: arcs, diffuse aurora, proton aurora, pulsating aurora, black aurora, and auroral patches. Specifically, auroral activity will be correlated with conjugate in situ measurements of (a) particle losses from the electron plasma sheet, (b) particle losses from the outer ring current/partial ring current, (c) ion pressure release, (d) electron pressure release, (e) heating and cooling of the electron and ion plasma sheets, (f) increases or decreases of particle anisotropies, (g) ionospheric upflow of ions into the equatorial magnetosphere, and (h) ionospheric upflows of electrons into the equatorial magnetosphere.

4.D Field-line mapping dynamics.

Electron-spectra-matching tests between magnetospheric and low-altitude satellites indicate that magnetic-field models can be surprisingly bad at predicting the magnetic-field connections between the magnetosphere and the ionosphere [e.g. *Hones et al.*, 1996; *Weiss et al.*, 1997]. The reasons for the mapping by models being in error are not known.

MIO will provide unambiguous tests of our magnetic-field models. The scope of the tests would be larger, particularly if radar is used to locate the beamspot, enabling magnetic-field-model tests to be made at all local times. Such testing could lead to improvements in our magnetic-field models, particularly in the regions of the outer dipole, the outer radiation belt, the ring current, and the partial ring current.

With MIO, the temporal dynamics of magnetosphere-ionosphere connectivity could be systematically studied through substorm phases and through ring-current and partial-ring-current growth and decay. Correlations between changes in the mappings with such quantities as magnetospheric plasma- β could be made.

The effects of auroral field-aligned currents and auroral perpendicular flows on the magnetic-field connections between the magnetosphere and ionosphere could be studied, ascertaining such quantities as the total amount of magnetic shear across auroral arcs.

5. Facility Use and Campaign Possibilities

The Magnetosphere-Ionosphere Observatory can be used as a facility by the ionospheric and magnetospheric communities; its mode of operation can be changed to focus on particular scientific studies that may arise. And MIO can be used in coordinated campaigns with instruments fielded by the communities.

An example of facility use would be changing the satellite separations to study a particular science issue, such as widening the separations to study the shielding of convection electric fields (see Table 6).

Another example of facility use would be changing the orbits so that the diurnal dance (Figure 10) results in radial alignment with multiple radial separations of the satellites on the nightside to allow simultaneous multiple-scalesize gradients to be observed.

And another example of facility use would be to change the electron-gun operations so that “burst modes” could be triggered from the ground observatory when particularly interesting auroral activity is ongoing or when particularly interesting auroras are crossing the footprint.

By fielding ground-based instrumentation at the auroral observatory or by using conjunction data with other satellites, MIO can be used in campaigns for additional scientific studies of the aurora, the magnetosphere, and the ionosphere. Six examples are given in the six paragraphs below.

By fielding balloon-borne x-ray detectors under the ionospheric footprint and/or by using DMSP overflights of the ionospheric footprint, information about the energy spectra and fluxes of auroral electrons can be obtained, allowing correlations to be made between the properties of the auroral generator (as measured by the MIO satellites) and the voltage and current of the auroral accelerator (as analyzed from low-altitude electron-flux information).

Analyzing the data from ground-based magnetometer chains allows correlations to be made between magnetospheric magnetic-field distortions from dipole geometry (stretching and twisting as measured by the MIO satellites) and ionospheric closure currents (as determined from the magnetometer chains).

Fielding ground-based optical telescopes aimed into the local magnetic zenith in the vicinity of the ionospheric footprint allows correlations to be made between the presence of ultra-small-scale auroral structure and the conditions in the conjugate magnetosphere (as measured by the MIO satellites).

Operating ionospheric heaters at the ionospheric footprint allows the effects of ionospheric perturbations such as the lofting of heated electrons and the resulting ambipolar expansion plasma from the topside ionosphere into the magnetosphere to be diagnosed from the magnetosphere by the MIO satellites.

Fielding ground-based wave transmitters to launch ducted waves from the ionospheric footprint into the magnetosphere allows studies to be made of wave transmission through the

ionosphere and of wave propagation in the magnetosphere, if MIO carries a plasma-wave detector (see Table 3).

Fielding high-resolution wavelength-filtered cameras to look at the MIO beamspot in both a prompt emission line (3914-Å or 4278-Å) and the delayed emission line 5577-Å of atomic oxygen allows one to use the MIO beam to optically tag the neutral atmosphere and measure the neutral wind velocity at the altitudes of the optical beamspot.

6. EPO Themes

The MIO mission will be a resource for contributions to the EPO themes “seeing the invisible”, “magnetic fields”, “coupled system”, and “scales”. Aurora is the stuff of legends in the northern cultures, appearing as awesome moving structures in the atmosphere but created very far away. There is an accurate connection over long distances via the Earth’s magnetic field out in space between the aurora and its distant cause. Below are some examples of EPO themes.

Seeing the Invisible: In the classroom you can use iron filings to trace out the invisible magnetic-field lines around a dipole magnet to see where the field lines connect. If currents are turning on and off near the dipole, “where the field lines go” will change. In space, magnetic fields connect things together. For understanding cause and effect in space, knowing what is connected to what is crucial. In the magnetosphere-ionosphere system the iron-filings trick is not practical so we use the MIO electron gun as a tool to trace out the magnetic-field lines to see where they go. With changing currents out in the magnetosphere, which are uncontrolled, “where the field lines go” changes. It will be explained to the students and teachers that the motivation for NASA to go to the extreme effort to fly this gun is because it is the only way to determine what is magnetically connected to the upper-atmosphere auroras, i.e. it's the only way to see what is making auroras.

Magnetic fields: In space, magnetic fields connect things together. Magnetic fields also guide the orbits of charged particles. By firing an electron gun along the direction of the local magnetic field, the beam of electrons follows the curved magnetic field lines and hits the upper atmosphere, making an optically detectable spot 0.35 seconds after the beam fires. The electron gun out in space is not aimed at the Earth, but is aimed in the direction that the magnetic field points. This direction, which changes, is determined by onboard magnetic-field sensors.

Coupled System: The magnetosphere and the ionosphere are a coupled system, coupled by the magnetic field connection. When the auroral images at the satellite footpoint in the atmosphere change, there should be a change in the magnetosphere. A particularly clear example would be the edge of the diffuse aurora coming over the footpoint from the north in the late evening; simultaneous with this the hot-electron population of the edge of the electron plasma sheet in the magnetosphere sweeps radially inward over the satellites. This example has been successfully tested with an all-sky auroral camera located east of Fairbanks, Alaska and a geosynchronous satellite with an onboard electron detector [Suszcynsky *et al.*, 1998; Shum *et al.*, 2000]. A more-sophisticated example of the coupled magnetosphere-ionosphere system would be to see either the magnetosphere or the ionosphere dynamically change, and then a minute or so later see the other react to that change, showing a cause-and-effect in the magnetosphere-ionosphere system. (The minute-or-so time delay corresponds to the Alfvén-speed propagation of electrical signals through the magnetosphere.)

Scales: Example 1. The electron beam travels about 50,000 km in distance from the satellite to the atmosphere to make a beam spot that is only about 30-meters across. This is because of the

very precise guiding of the beam electrons by the magnetic field. If this were to be scaled down so that the flight distance was only 1 km, then the beamspot would be 0.6-mm wide, which is about the size a period in this 12-point typeface. Example 2. There are different scales in the magnetosphere and the atmosphere caused by the convergence of magnetic-field lines near the Earth. In the upper atmosphere two magnetic-field lines are relatively close together. Those two magnetic-field lines are further apart in the magnetosphere. A north-south separation of 1 km in the upper atmosphere maps to a 33-km radial separation in the geosynchronous equator 41,000 km from the Earth's center. And a east-west separation of 1 km in the atmosphere maps to a 17-km azimuthal separation in the geosynchronous equator. Thus to measure aurora structures with one scale size in the upper atmosphere, satellite separations that are much larger than that size must be used in the magnetosphere.

7. Summary

The Magnetosphere-Ionosphere Observatory (MIO) is a mission concept high on quantitative science. It is designed to bring closure to the important question: ***How does the magnetosphere generate auroral arcs?*** Answering this question will allow us to discern the impact that the aurora has on the evolution and dynamics of the magnetosphere, and it will allow us to build a comprehensive model for auroral arcs.

MIO will also solve other important science issues dealing with (1) magnetosphere-ionosphere coupling, (2) the causes of other types of aurora, (3) the impacts of all types of aurora on the magnetosphere, and (4) magnetic-field-line mapping.

MIO has some unique advantages. MIO will truly yield magnetospheric and ionospheric measurements that are conjugate. MIO will produce spatial and temporal measurements in the magnetosphere connected to spatial and temporal measurements in the ionosphere. Lots of such conjunction data will be obtained, and the satellites will visit interesting regions of the magnetosphere.

Technology wise, MIO is ready.

MIO is a facility geared to the science of the magnetospheric, ionospheric, and auroral communities with opportunities to mount campaigns utilizing ground-based and balloon-borne instrumentation and other-satellite magnetic conjunctions.

8. Personnel

The following individuals helped to develop the MIO mission concept [cf. *Borovsky et al.*, 1998, 2000].

Phil Barker	Los Alamos National Laboratory
Joachim Birn	Los Alamos National Laboratory
Joe Borovsky	Los Alamos National Laboratory
Jim Burch	Southwest Research Institute
Mike Collier	NASA/Goddard Space Flight Center
Jim Cravens	Southwest Research Institute
Reiner Friedel	Los Alamos National Laboratory
Ray Greenwald	Johns Hopkins/Applied Physics Laboratory
Tom Hallinan	University of Alaska, Fairbanks
Jim Horwitz	University of Alabama, Huntsville
Herb Funsten	Los Alamos National Laboratory
Mike Kelley	Cornell University
Dave Klumpar	Montana State University, Bozeman
Bob Lysak	University of Minnesota, Minneapolis
Barry Mauk	Johns Hopkins/Applied Physics Laboratory
Dave McComas	Southwest Research Institute
Steve Mende	University of California, Berkeley
Tom Moore	NASA/Goddard Space Flight Center
Craig Pollock	Southwest Research Institute
Tuija Pulkkinen	Finnish Meteorological Institute
John Raitt	Utah State University, Logan
Geoff Reeves	Los Alamos National Laboratory
Howard Singer	NOAA/Space Environment Laboratory
Jan Sojka	Utah State University, Logan
Pekka Tanskanen	University of Oulu
Don Thompson	Utah State University, Logan
Michelle Thomsen	Los Alamos National Laboratory
Brent White	Space Dynamics Laboratory

Appendix A: Optical Spotting of the Illuminated Footpoint

A.1. Spot Optical Power

Dalgarno et al. [1965] quote (Hartman and Hoerlin) that the efficiency for converting electron beam energy in 3914Å photon energy (at low pressures) is about 3.7×10^{-3} . As an example, a 10 kilowatt electron beam will produce 30 watts of 3914-Å emission in the atmosphere. This estimation of the beam-spot optical power P_{spot} neglects the effects of backscattering of the beam electrons off the atmosphere, which removes energy (power) that would be available to excite the optical emissions. About 15% of the beam energy is not deposited in the atmosphere owing to backscatter back into space.

A.2. 3914Å versus 4278Å

The first negative band of N_2^+ (which is excited when an N_2 molecule is ionized by the passage of a fast electron) has heads near 4709Å (0,2), 4278Å (0,1), and 3914Å (0,0) [Stewart, 1958]. *Green and Barth* [1965] have the calculated relative intensities for those three bands at 11:38:100, respectively, for excitation by 30-keV electrons. (These ratios should be more-or-less independent of the electron beam energy, provided the beam energy is above about 500 eV.) This means that 3914Å is $100/38 = 2.6$ times as bright as 4278Å. For example, if the beam spot is 30 watts in the 3914-Å band, then it is about 11.4 watts in the 4278-Å band.

Although longer-wavelength optical photons are transmitted through the air with little attenuation, shorter-wavelength optical photons are not (see, for instance, Figure 3 of *Prueitt* [1963]). The intensity I of light as it propagates can be described by $I = I_0 e^{-\kappa x}$, where x is the distance (sea-level equivalent) it has propagated and κ is the attenuation coefficient. The value of κ depends on the wavelength of the light and on the amount of aerosols in the air. If there are no aerosols, then the attenuation is chiefly owed to Rayleigh scattering. For 3914-Å light, $\kappa \approx 0.044 \text{ km}^{-1}$ for no aerosols [Penndorf, 1957; ITT, 1977], i.e. for Rayleigh scattering. For a vertical propagation through 760 Torr of air, which is about 10.3 km of sea-level-equivalent air, the attenuation coefficient is $e^{-0.453} = 0.635$, which is a loss of 36% of the photons owing to Rayleigh scattering. At a wavelength of 4278Å, the Rayleigh scattering is less severe (the attenuation coefficient goes as λ^{-4}). The scattering loss is more severe for airglow that is not vertically overhead because of the passage through more air. The amount of Rayleigh-scattering atmospheric

attenuation of 3914-Å and 4278-Å emission coming from the topside of the atmosphere are plotted as functions of the viewing angle from the zenith in Figure 12. As can be seen, out to a viewing angle of 60° , the difference in attenuation between the two wavelengths is only 30% or less. With the presence of aerosols, the attenuation increases for both wavelengths [see, for instance, *ITT*, 1977], but the increase is greater for 4278Å so that the difference in attenuation between the two wavelengths lessens.

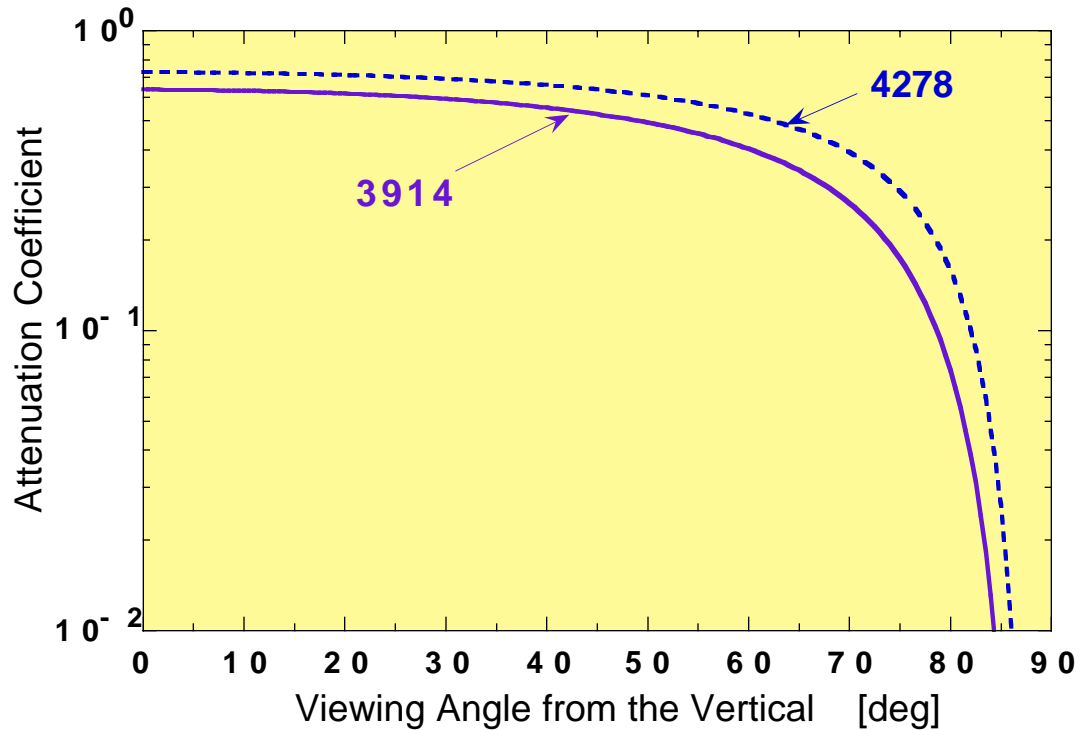


Figure 12. The attenuation coefficient for 3914-Å and 4278-Å light passing through the entire atmosphere to the ground, plotted as a function of the ground viewing angle (slant angle) from vertical.

A.3. Dimensions of the Optical Spot

Particle-trajectory simulations were run for magnetized, electrons precipitating onto the top of the atmosphere undergoing angular scattering and dE/dx energy loss in the atmospheric gas using the methodology outlined in Appendix 1 of *Borovsky et al.*, [1991]. The energy from a "point" beam is deposited into a tall cylinder aligned along the magnetic field which emits photons owing to air excitations. In Figures 5, 6, and 4 the vertical, horizontal, and cross-sectional and profiles of the cylinder of emission of a 60-keV electron beam. In these figures, the beam electrons were taken to be isotropic as they entered the top of the atmosphere (i.e. the beam angular width filled loss cone). As can be seen in Figure 6, the horizontal width of the beamspot is about 30 meters. The gyroradius of an electron in a 0.6-gauss magnetic field is $r_{ge} \sim 1.8 \text{ m } E_{kev}^{1/2}$, where

E_{kev} is the energy of the electron expressed in keV and where the velocity is entirely perpendicular to the magnetic field. For a 60-keV electron the gyroradius is about 14 meters. As can be seen in the figure, half of the emission comes from a cylinder that has a half-width that is about one beam-energy gyroradius. An emitting cylinder with this small radius will not be resolved by a camera (see below). Note that this small half width only applies to emission from a line or band that is prompt, such as are the 3914-Å and 4278-Å band emissions. For a slow emission such as 5577Å, smearing of the beamspot by neutral winds will significantly enlarge the emitting region [Borovsky, 1993].

As can be seen in the height profiles of the beamspot optical emission plotted in Figure 5, half of the beam optical emission occurs from a cylinder that is ~7 km tall along the magnetic field. This height profile does not drastically change if the beam does not fill the loss cone.

Hence, the particle-trajectory simulations indicate the energy deposition by the electron beam in the atmosphere produces a cylinder of optical emission that is about 7-km tall and about 7 m in diameter.

A.4. Photons per Pixel of a CCD Camera from Aurora

In this and the following two sections, the problem of seeing a beamspot against the background of a moderate-intensity auroral arc will be considered. The number of photons per pixel of a CCD camera will be calculated for the beam source N_{beam} and for the aurora source N_{aurora} , and it will be found that the beam signal is out of the background noise, i.e. it will be found that $N_{\text{beam}} > N_{\text{aurora}}^{1/2}$.

The background aurora is taken to have a brightness B_{aurora} in the emission band of interest (i.e. in the 3914-Å bandhead or the 4278-Å bandhead), where B_{aurora} is expressed in units of Rayleighs (R), with $1 \text{ R} = 10^6 \text{ photons/cm}^2/\text{sec}$ being emitted isotropically from the sky, where the cm^2 is an element of area on the sky as seen from the camera. If the aurora is a distance d from the camera, and if the camera lens has an aperture with a radius r_{aper} , then the fraction F of the photons emitted isotropically by the aurora in the sky that enter the aperture of the camera is

$$F = (\pi r_{\text{aper}}^2) / (4\pi d^2) = r_{\text{aper}}^2 / 4d^2 . \quad (1)$$

(Note that F is a number of the order of 10^{-8} - 10^{-12} .) Denoting the focal length of the lens as L , the pixel (register) size on the CCD array as Δx_{ccd} , and the "pixel" size (resolution element) on the sky at the distance d of the aurora as Δx_{sky} , the conservation of angles through the lens gives

$$\Delta x_{\text{ccd}} / L = \Delta x_{\text{sky}} / d , \quad (2)$$

which gives

$$d = L \Delta x_{\text{sky}} / \Delta x_{\text{ccd}} \quad . \quad (3)$$

Using this expression to eliminate d in the above expression for F , and using the definition of the f -number of the lens

$$f = L / 2r_{\text{aper}} \quad (4)$$

to eliminate d yields the expression

$$F = (1 / 16f^2) (\Delta x_{\text{ccd}}^2 / \Delta x_{\text{sky}}^2) \quad (5)$$

for the fraction of emitted photons that reach the camera aperture.

The total number of photons (in the band) emitted from one "pixel" of aurora in the sky during a time Δt is

$$N = B_{\text{aurora}} 10^6 \Delta t \Delta x_{\text{sky}}^2, \quad (6)$$

where the factor of 10^6 comes in because the brightness of the aurora B_{aurora} is expressed in units of Rayleighs. Any photon emitted from this pixel of the sky that hits the aperture of the lens will be focused into the appropriate pixel (register) of the CCD array. Hence, the number of photons N_{aurora} emitted by the aurora that go into a pixel of the CCD camera is given by $N_{\text{aurora}} = NF$, which is

$$N_{\text{aurora}} = B_{\text{aurora}} 10^6 \Delta t \Delta x_{\text{sky}}^2 F \quad (7)$$

Using expression (5) for F in expression (7) yields

$$N_{\text{aurora}} = B_{\text{aurora}} \Delta t (10^6 / 16f^2) \Delta x_{\text{ccd}}^2. \quad (8)$$

For an example, a fairly bright auroral arc with a total (all-wavelengths) brightness of 70-100 kR (kiloRayleighs) will be taken. If the total brightness of the arc is 70-100 kR, then the 3914-Å brightness is $B_{\text{aurora}} = 15 \text{ kR}$ [Dalgarno *et al.*, 1965; Omholt, 1971]. If one pixel of the CCD has size of $\Delta x_{\text{ccd}} = 2 \times 10^{-3} \text{ cm}$ [Photometrics, 1990], if the f -number of the lens is $f = 2$, and if the exposure time is taken to be $\Delta t = 0.5 \text{ sec}$, then the number of photons per CCD pixel owed to the bright background of aurora is $N_{\text{aurora}} = 470 \text{ photons}$.

A.5. Photons per Pixel of a CCD Camera from Beamspot

As was discussed in Section C above, half of the optical power P_{beam} of the beamspot is emitted from a cylinder that has a height Δh of about 4 km and a radius of a few meters. For pixel resolution Δx_{sky} on the sky that is a fraction of a km, the radius of the cylinder will not be resolved but the height will. In that case, the optical power emitted per sky pixel that contains part of the

beamspot cylinder is

$$P_{\text{pixel}} = 0.5P_{\text{beam}}\Delta x_{\text{sky}}/(\Delta h \sin\theta) , \quad (9)$$

where θ is the viewing angle to the pixel in the sky pixel as measured from the vertical direction and where the factor of 0.5 accounts for the fact that half of the beam power is emitted from Δh . (Note that this expression breaks down at the vertical where the unresolved beamspot goes into only one pixel, i.e. is valid only for $\Delta x_{\text{sky}} > \Delta h \sin\theta$.) The total rate \mathfrak{R} of photon emission (isotropically) from the portion of the beamspot cylinder that resides in one sky pixel is $\mathfrak{R} = P_{\text{pixel}}/E_{\text{photon}}$, where E_{photon} is the energy of a single photon. For 3914Å, $E_{\text{photon}} = 3.17 \text{ eV} = 5.1 \times 10^{-12} \text{ erg}$. Using expression (9), this rate is

$$\mathfrak{R} = (0.5P_{\text{beam}}/E_{\text{photon}}) (\Delta x_{\text{sky}}/(\Delta h \sin\theta)) , \quad (10)$$

which has units of photons/sec. The brightness B_{beam} (in units of Rayleighs) of the unresolved beam (i.e. the beam brightness diluted into a full sky pixel) is $B_{\text{beam}} = 10^{-6} \mathfrak{R}/\Delta x_{\text{sky}}^2$, where the factor of 10^{-6} comes from the definition of a Rayleigh (see Section D above). Using expression (10), this is

$$B_{\text{beam}} = 10^{-6} (0.5P_{\text{beam}}/E_{\text{photon}}) (\Delta x_{\text{sky}}/(\Delta h \sin\theta)) \Delta x_{\text{sky}}^{-2} \quad (11)$$

As an example, taking $P_{\text{beam}} = 30 \text{ Watts} = 3 \times 10^8 \text{ erg/sec}$, $E_{\text{photon}} = 5.1 \times 10^{-12} \text{ erg}$, $\Delta x_{\text{sky}} = 0.5 \text{ km} = 5 \times 10^4 \text{ cm}$, $\Delta h = 4 \text{ km} = 4 \times 10^5 \text{ cm}$, and $\theta = 30^\circ$, expression (11) yields an equivalent beam brightness in the pixel of $B_{\text{beam}} = 2940 \text{ R}$ at 3914Å. In these pixels, the beamspot is about 20% as bright as the moderate-intensity arc considered in Section D above ($B_{\text{aurora}} = 15 \text{ kR}$ at 3914Å), but it is significantly brighter than the diffuse-aurora background, which is 1 kR or less in 3914Å when present [Omholt, 1971].

The number of photons N_{beam} that the beamspot contributes to a pixel (register) of the CCD camera is given by expression (8) with B_{beam} substituted for B_{aurora} ,

$$N_{\text{beam}} = B_{\text{beam}} \Delta t (10^6/16f^2) \Delta x_{\text{ccd}}^2 . \quad (12)$$

For an example, taking $B_{\text{beam}} = 2940 \text{ R}$, $\Delta x_{\text{ccd}} = 2 \times 10^{-3} \text{ cm}$, $f = 2$, and $\Delta t = 0.5 \text{ sec}$, then the number of photons per CCD pixel owed to the beamspot is $N_{\text{beam}} = 92 \text{ photons}$.

A.6. Comparing the Beamspot Signal to the Auroral Background

For the example parameters used in Sections D and E, the number of photons per CCD pixel for the auroral arc was found to be $N_{\text{aurora}} = 480 \text{ photons}$ and the number of photons per CCD pixel for the beamspot was found to be $N_{\text{beam}} = 92 \text{ photons}$. For these values, the desired

condition $N_{\text{beam}} > N_{\text{aurora}}^{1/2}$ discussed in Section D is $92 > 22$, which is met. Hence, for the example parameters given, the beam spot can be discernible even against a background of a moderate-intensity auroral arc in the same pixels. Taking into account that the beam will make a coherent multi-pixel streak of enhanced counts in each pixel, and using beam-on beam-off image comparisons, the seeing of the beam against an auroral-airglow background becomes more certain. If a realistic photon efficiency of the CCD camera is included, the $N_{\text{beam}} > N_{\text{aurora}}^{1/2}$ condition would still be satisfied. For instance, if the CCD efficiency ϵ for detecting a photon is 50%, then N_{beam} and N_{aurora} are both reduced by 0.5 so N_{aurora} becomes 240 counts and N_{beam} becomes 46 counts. In that case $N_{\text{beam}}/N_{\text{aurora}}^{1/2} = 46/15 \sim 3$, which is considerably above 1.

Defining the “goodness” G of the beamspot signal to the background auroral signal as $G = N_{\text{beam}}/N_{\text{aurora}}^{1/2}$, with $G \gg 1$ being desirable, expressions (12), (11), and (8) combine to give

$$G = 1.25 \times 10^{-4} (P_{\text{beam}} \Delta t^{1/2} / B_{\text{aurora}}^{1/2}) \epsilon^{1/2} \times (1/E_{\text{photon}} \Delta h \sin \Delta \theta) (\Delta x_{\text{ccd}} / \Delta \text{sky}) (1/f) , \quad (13)$$

where the CCD photon efficiency ϵ is included into the expression. The units to use in expression (13) are cgs (i.e. ergs and cm), with the auroral brightness B_{aurora} expressed in Rayleighs. Two parameters in expression (13) are not variable: E_{photon} and Δh . As can be seen from expression (13), choosing a camera that well resolves the sky (decreasing Δsky), that has a low f-number (decreasing f), and that has CCD pixels tied together (increasing Δx_{ccd}) are desirable to increase G .

Appendix B: Beam Divergence and the Loss Cone

B.1. Introduction

The main objective of the electron beam on MIO is for the beam to leave the gun on the satellite and deposit its kinetic energy into the upper atmosphere at the magnetic footpoint of the satellite. To deposit its energy in the atmosphere, the beam must be shot into the atmospheric loss cone. This involves pointing the beam in the right direction, and ensuring that the beam keeps a narrow angular spread so that it fits into the loss cone. One major limitation on keeping the angular divergence of the beam small is owed to the fact that the beam has a nonzero space charge, which produces a radial electric field, which causes the charged beam to expand radially as it propagates through space. This radial expansion can be surprisingly strong and it changes the pitch angles of the electrons in the beam. In this writeup, the angular spread of the propagating beam in the MIO mission will be calculated and compared with the size of the loss cone. The goal of this exercise is to adjust the parameters of the beam such that it fits into the loss cone.

B.2. The size of the loss cone

At geosynchronous orbit near the equator, the magnetic-field strength is typically about 80 - 120 nT, which, with $1 \text{ nT} = 10^{-5} \text{ gauss}$, is $8 \times 10^{-4} - 1.2 \times 10^{-3} \text{ gauss}$ [Fairfield and Takahashi, 1991]. On the dayside the magnetic field is typically stronger than it is on the nightside owing to the compression of the magnetosphere on the dayside and the stretching into a tail on the nightside. The magnetic-field strength at the Earth in the auroral zone is typically in the range of 0.5 - 0.6 gauss

[e.g. Fig. 4-11 of Jursa, 1985]. The half-angle θ of the loss cone as seen from the geosynchronous equator can be expressed

$$\sin \theta_{lc} = \left(\frac{B_{\text{equat}}}{B_{\text{atmos}}} \right)^{1/2} \quad (1)$$

as, e.g. expression (60) of Alfvén and Fälthammar [1963], where B_{equat} is the field strength at geosynchronous orbit and B_{atmos} is the field strength in the atmosphere. Using the ranges $B_{\text{equat}} = 8 \times 10^{-4} - 1.2 \times 10^{-3} \text{ gauss}$ and $B_{\text{atmos}} = 0.5 - 0.6 \text{ gauss}$ yields $\theta_{lc} = 2.1^\circ - 2.8^\circ$ for the half-angle of the loss cone as seen from the geosynchronous orbit. On the nightside of the orbit, the loss cone is toward the smaller end of this range, and on the dayside of the orbit, the loss cone is toward the

larger end of this range.

B.3. Beam-Propagation Effects in Vacuum

After the electron beam leaves the gun, the beam evolves because of several effects. In this section, the effects that will be included for a beam that is fired along the Earth's magnetic field \vec{B}_0 are: (1) the electrostatic radial expansion of the beam owing the space charge of the beam, (2) the $\vec{v} \times \vec{B}_0$ Lorentz force owing to the of the beam expanding across the Earth's magnetic field \vec{B}_0 , (3) the pinch force owing to the $\vec{v}_{\text{beam}} \times \vec{B}_{\text{self}}$ Lorentz force of the azimuthal self magnetic field \vec{B}_{self} of the beam, and (4) the relativistic-mass effect which retards the transverse accelerations of the beam electrons. In this section the beam will be assumed to propagate through a vacuum.

The electrostatic expansion of the beam in vacuum is associated with the radial electric field E_r arising from the charge of the beam. For a long cylindrical beam, the radial electric field in the vicinity of the beam is given by (in cgs units)

$$E_r = \frac{Q}{L} \frac{2}{r} \quad (2)$$

where Q/L is the charge per unit length of the beam interior to the radius r . Taking r to be the radius of the outer edge of the beam, Q/L is the total charge per unit length of the beam. For a beam with a current I_{beam} and a velocity v_{beam} , the charge per unit length of the beam is

$$\frac{Q}{L} = \frac{I_{\text{beam}}}{v_{\text{beam}}} \quad (3)$$

Accordingly, expression (2) becomes

$$E_r = \frac{2I_{\text{beam}}}{v_{\text{beam}} r} \quad (4)$$

The electrostatic force \vec{F}_E on an electron (with charge e) at the edge of the beam is $\vec{F}_E = eE_r \hat{r}$, which is

$$\vec{F}_E = \frac{2eI_{\text{beam}}}{v_{\text{beam}} r} \hat{r} \quad (5)$$

radially outwards.

As an electron gains a radial velocity owing to electrostatic repulsion, the $\vec{v} \times \vec{B}_0$ Lorentz force of the Earth's magnetic field will change the direction of the electron, tending to turn the radial velocity into an azimuthal velocity and then turning that azimuthal velocity into a radial velocity, and so on. This Lorentz force will limit and then reverse the expansion of the beam.

As will be seen below, the time to turn the expansion around into a contraction is approximately one-half of an electron gyroperiod in the Earth's magnetic field, which for a mildly relativistic beam and a field strength of 100 nT is about

1.8×10^{-4} sec. For a beam propagating along the Earth's magnetic field \vec{B}_o , the Lorentz force associated with the radial and azimuthal velocity of a beam electron is

$$\vec{F}_{\text{mag}} = -\frac{e}{c} \vec{v} \times \vec{B}_o \quad (6)$$

The current I_{beam} of the charged beam produces an azimuthal magnetic field (the self field) B_{self} with a strength at the outer edge of the beam that is

$$B_{\text{self}} = \frac{2I_{\text{beam}}}{c r} \quad (7)$$

where r is the radius of the outer edge of the beam. A beam electron moving with an axial velocity v_{beam} across this azimuthal self field sees a radially inward Lorentz force

$$\vec{F}_{\text{pinch}} = -\frac{2e v_{\text{beam}} I_{\text{beam}}}{c^2 r} \vec{r} \quad (8)$$

which is known as the pinch force [Miller, 1982]. For an unneutralized beam, the radially inward pinch force is always less than the radially outward electrostatic-repulsion force. This is seen by using expression (5) and (6) to form the ratio F_E/F_{pinch} , which gives

$$\frac{F_E}{F_{\text{pinch}}} = \frac{v_{\text{beam}}^2}{c^2} \quad (9)$$

which must always be less than unity.

Since it may be the case that v_{beam} is not extremely small compared with the velocity of light c (e.g. for a 100-keV beam, $v_{\text{beam}}/c = 0.625$), the equations of motion for beam electrons undergoing the electrostatic-repulsion force, the Lorentz force, and the pinch force will be formulated relativistically. The equation of motion can be written [e.g. Goldstein, 1981]

$$\frac{d}{dt}(\gamma m \vec{v}) = \vec{F}_E + \vec{F}_{\text{mag}} + \vec{F}_{\text{pinch}} \quad (10)$$

where $\gamma = (1 - \beta^2)^{-1/2}$, where $\beta = v/c$, where v is the total velocity of a beam electron. Denoting the transverse velocity of a beam electron as v ,

for $v \ll v_{\text{beam}}$, $\beta \approx v_{\text{beam}}/c$. If the transverse velocity remains small compared with the beam velocity v_{beam} (i.e. if the divergence angle remains small), then the $\vec{v} (d\gamma/dt)$ term can be neglected compared with the $\gamma(d\vec{v}/dt)$ term on the left-hand side of expression (10), and expression (10) becomes

$$\frac{d\vec{v}}{dt} = \frac{1}{m\gamma} [\vec{F}_E + \vec{F}_{\text{mag}} + \vec{F}_{\text{pinch}}] \quad (11)$$

For $0 \leq \mathcal{E}_{\text{beam}} \leq 100$ keV, the value of gamma is $1 \leq \gamma \leq 1.28$. The second equation of motion is

$$\frac{d\vec{x}}{dt} = \vec{v} \quad (12)$$

For a cylindrically symmetric electron beam, the equations of motion (11) and (12) for an electron at the outer edge of the beam are computationally solved with a simple finite-difference scheme in double precision, reducing the timestep until no change in accuracy results. The forces going into expression (11) are obtained from expressions (5), (6), and (8). Effects that are not included are (1) any non-azimuthal symmetry to the beam, (2) the curvature of the Earth's magnetic field, and (3) dynamic shielding of the beam by the background magnetospheric plasma. (The dynamic shielding is discussed in the next section.) The results of the computations are displayed in Figures B1-B7. Most of the computations will deal with a 10-kilowatt beam that has an energy $\mathcal{E}_{\text{beam}} = 60$ keV (which means a velocity $v_{\text{beam}} = 1.45 \times 10^{10}$ cm/sec and a relativistic factor $\gamma = 1.14$, a current $I_{\text{beam}} = 0.166$ amp, an initial radius $r_0 = 1$ cm, propagating along a magnetic field $B_0 = 100$ nT = 1×10^{-3} gauss).

In Figure B1 the radius r_{beam} (left axis) and radial velocity v_{beam} (right axis) of the outer edge of the beam is plotted as a function of time. The initial perpendicular velocity (as the beam exits the gun) is taken to be zero. As can be seen, very rapidly the beam picks up a substantial perpendicular velocity owing to the electrostatic repulsion of the beam electrons and the beam begins to expand in radius. The expansion is halted and reversed by the Lorentz force $\vec{v} \times \vec{B}_0$ of the electron motion across the Earth's magnetic field \vec{B}_0 . The expansion is halted after a time that is slightly more than one-half of an electron gyroperiod in the Earth's field, where the gyroperiod τ_{ce} is given relativistically by $\tau_{ce} = 2\pi\gamma mc/eB_0$ [e.g. *Alfven and Falthammar*, 1963]. For $B_0 = 1 \times 10^{-3}$ gauss and $\gamma = 1.14$, the cyclotron period is $\tau_{ce} = 4.1 \times 10^{-4}$ sec. The beam repeatedly expands and collapses with a period that is slightly larger than a gyroperiod.

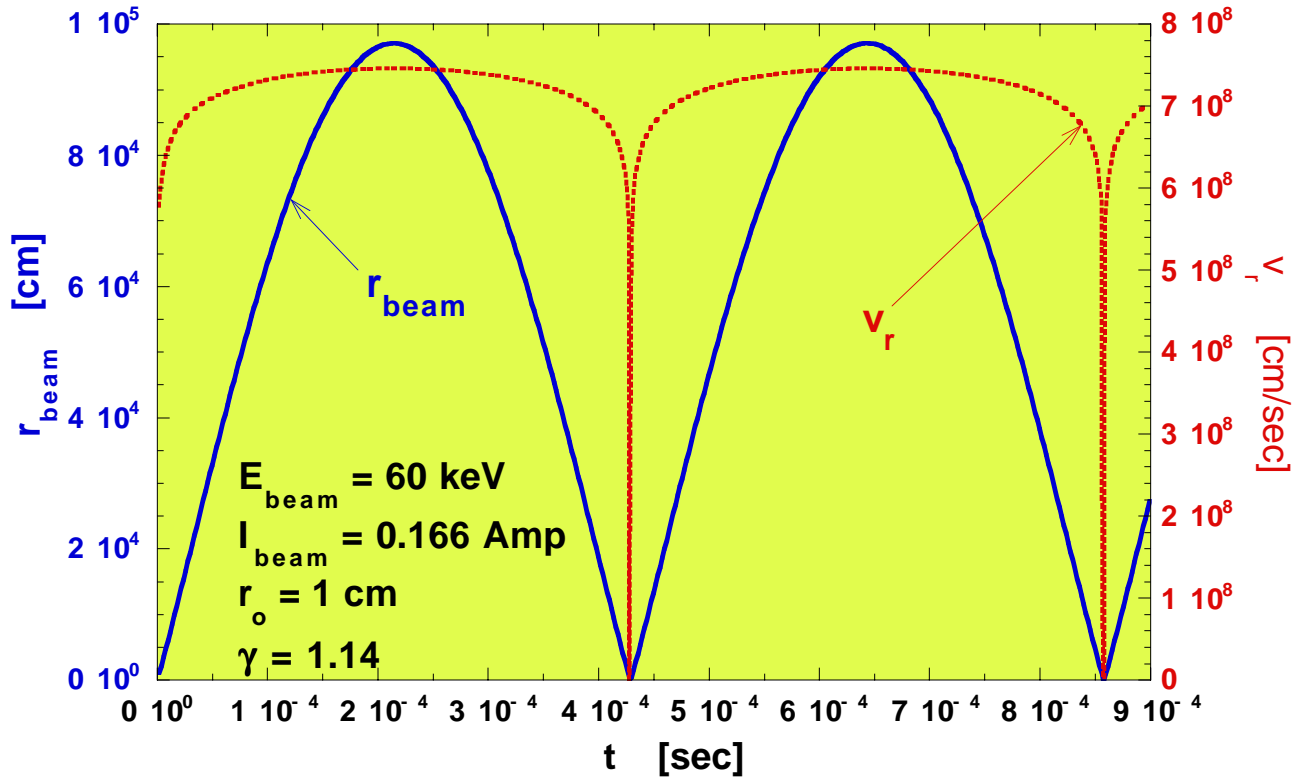


Figure B1. From a computer simulation of the radial expansion of the MIO electron beam, the beam's outer radius (blue, left axis) and the beam's radial velocity at the outer edge (red, right axis) are plotted as function of time.

In Figure B2, the transverse motion of a single electron on the beam edge is plotted for the initial 9×10^{-4} sec of motion. The magnetic field \vec{B}_o of the Earth points into the page. The center of the beam is at $x = 0, y = 0$. The direction of motion is labeled with arrowheads and the sequential position of the electron is labeled with numbers 1 - 7. Along with a periodic radial motion outward and inward, the electron continually rotates in one direction around the beam, in the $\vec{E} \times \vec{B}_o$ direction, where \vec{E} is the radially inward electrostatic field of the beam's space charge.

Transverse Motion of Electron on Beam Edge

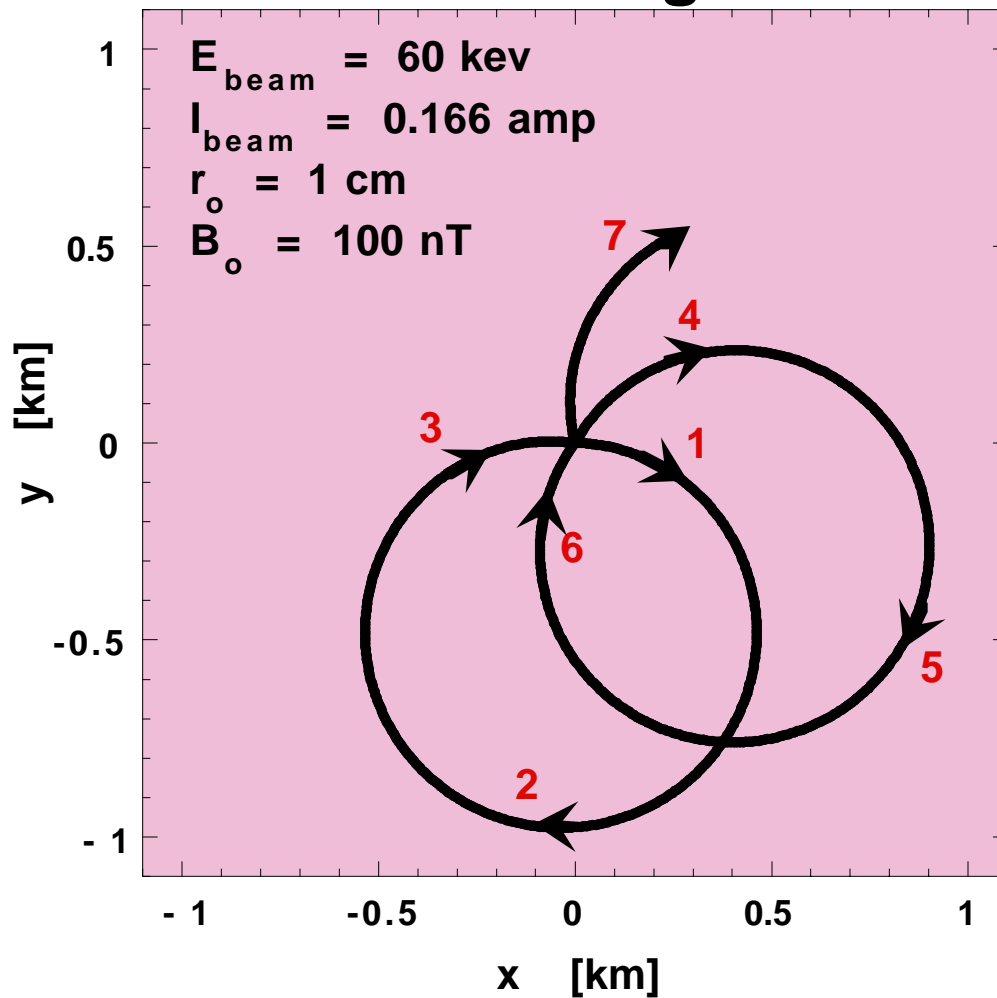


Figure B2. From a computer simulation of the MIO beam, the motion of a single electron on the beam edge is drawn transverse to the beam. The ambient magnetic field points into the page.

In Figure B3, the number density of the beam is plotted as a function of time. As the beam periodically increases and decreases in radius, the number density of the beam decreases and increases. When the beam is fully expanded, the density is much less than the typical density of the magnetospheric plasmas ($\sim 10^{-1} - 1 \text{ cm}^{-3}$) and when the beam is fully contracted its density is much greater than the typical magnetospheric densities. Most of the time, the beam density is less than the ambient density.

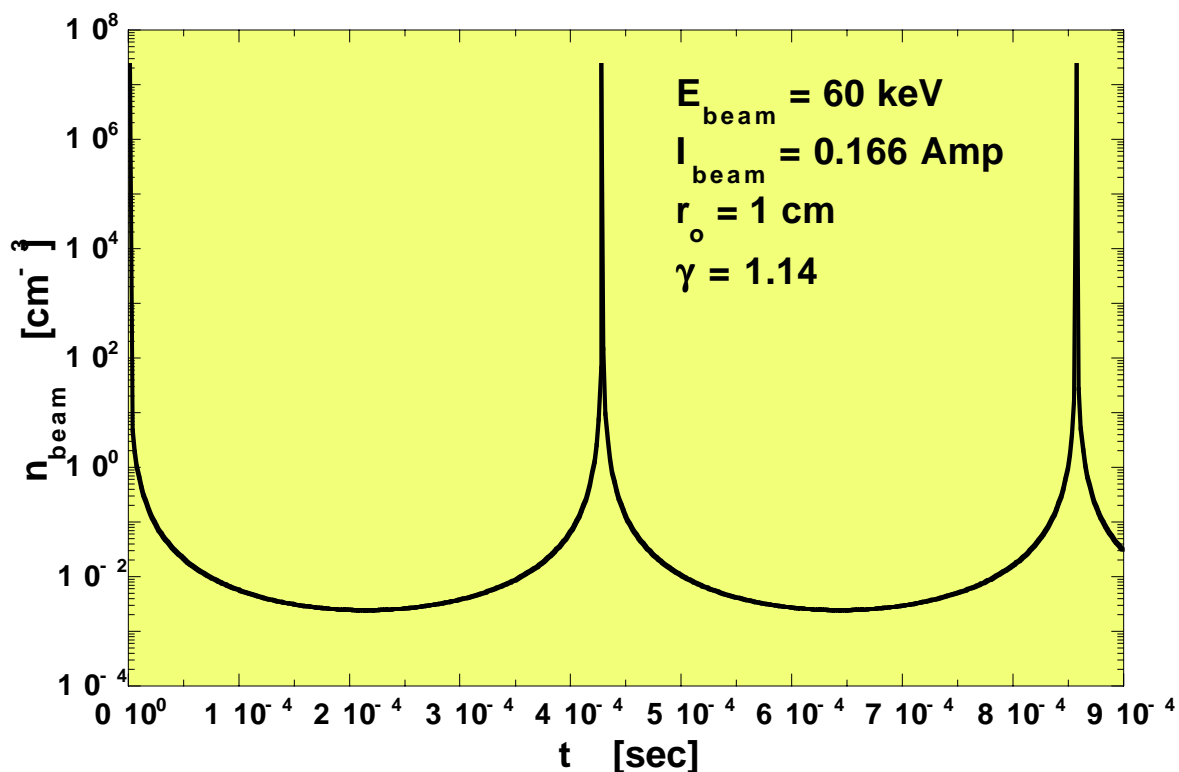


Figure B3. From a computer simulation of the transverse dynamics of the MIO beam, the beam number density is plotted as a function of time.

In Figure B4, the pitch angle of an electron at the outer edge of the beam is plotted as a function of time. As the perpendicular velocity of the electron increases and decreases, the pitch angle increases and decreases. As can be seen, the electron spends most of its time at a pitch angle that is close to the maximum pitch angle.

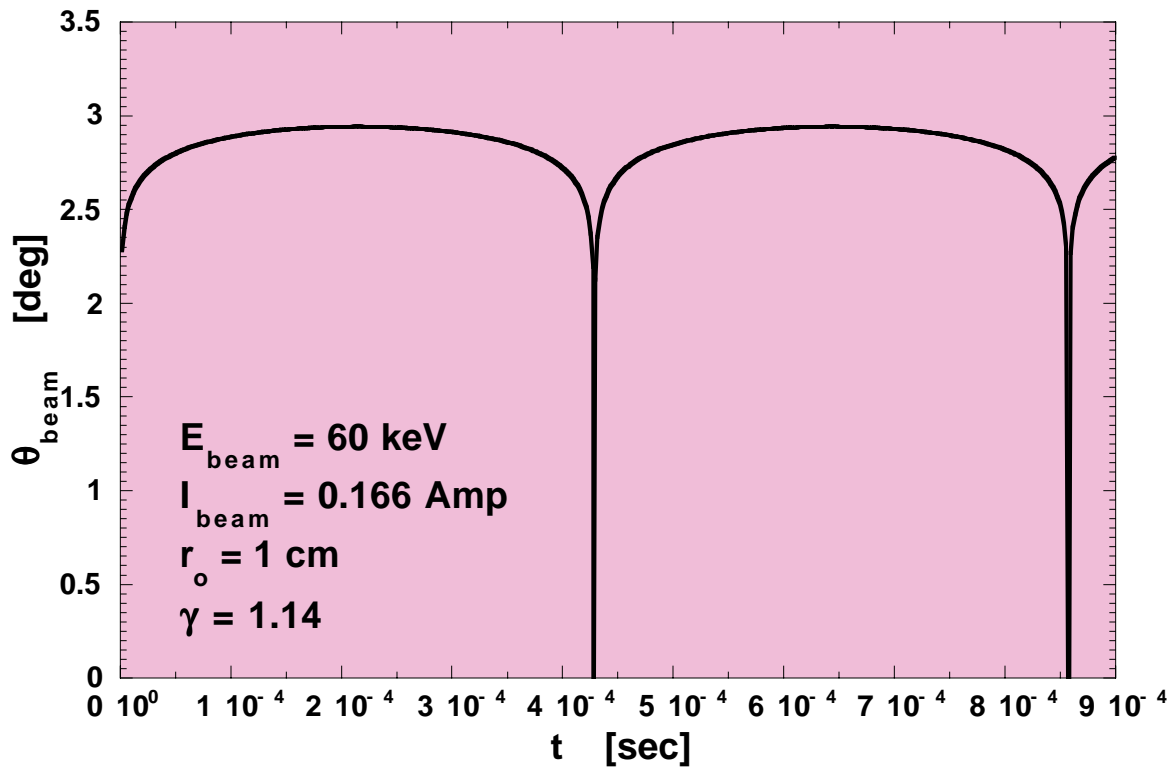


Figure B4. From a computer simulation of the transverse dynamics of the MIO beam, the divergence angle of the beam is plotted as a function of time.

Electrons internal to the beam (those not at the outer edge of the beam) will obtain pitch angles that are less than the pitch angles of the outer-edge electrons. In Figure B5 the distribution of maximum pitch angles obtained for the distribution of electrons in the beam is plotted. Electrons residing near the beam center (where, really, there are relatively few electrons) pick up only small pitch angles since the radial electric fields are weakest at the beam center, and electrons residing near the beam outer edge (where there are greater numbers of electrons) pick up larger pitch angles since the radial electric fields are strongest there.

Angular Distribution of the MIO Beam

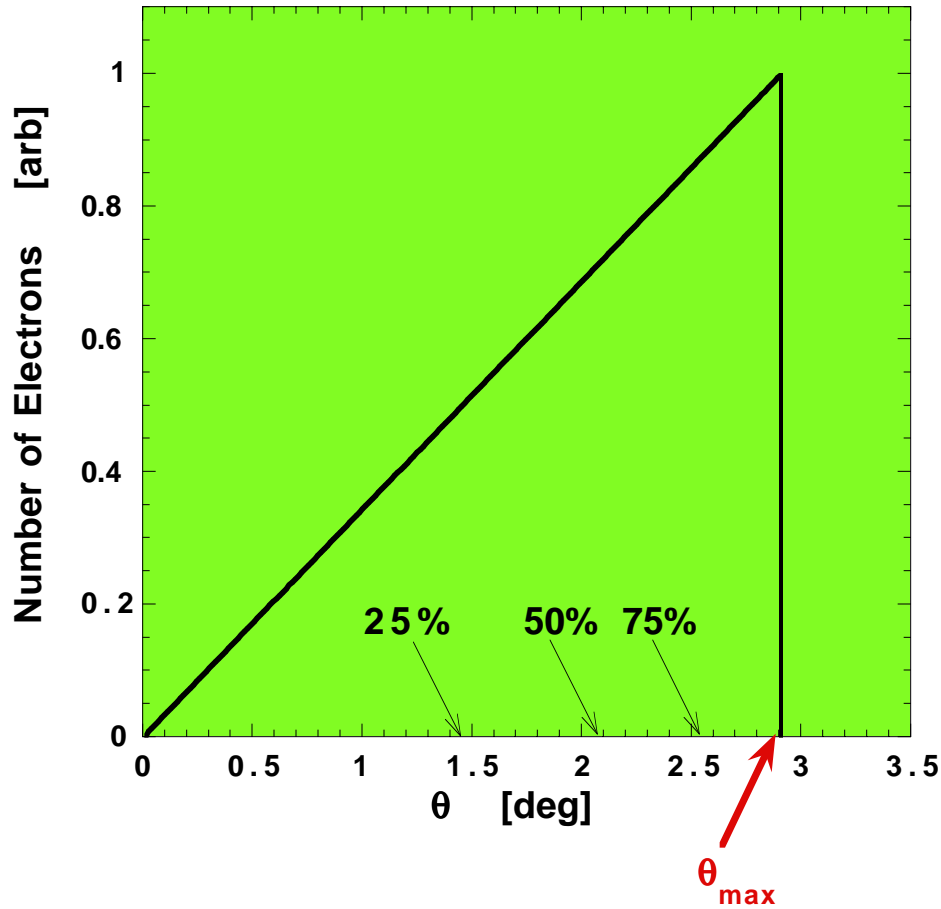


Figure B5. For a beam that is azimuthally symmetric, the distribution of divergence angles of electrons in the beam is plotted. For a field-aligned beam, the distribution of divergence angles is the distribution of pitch angles.

In Figure B6, the maximum divergence angle (= pitch angle) obtained by an electron at the outer edge of the beam is plotted as a function of the energy of the beam $\mathcal{E}_{\text{beam}}$ for three different values of the beam power $P = \mathcal{E}_{\text{beam}} I_{\text{beam}}$. In all cases, the initial radius of the beam (at the gun exit) is $r_0 = 1$ cm. As can be seen, for a given power, a higher-energy beam has a reduced maximum divergence angle (and so, a reduced spread in pitch angles). In Figure B6 the range of values for the atmospheric loss cone as seen from the geosynchronous-orbit equator is indicated by the two horizontal dashed lines. For the gun-emitted beam to fit into the loss cone, the maximum pitch angle that the beam obtains must be less than the value of the loss cone. Comparing the top horizontal line (2.8°) with the three curves, if the beam has a power of 1 kilowatt then the gun must have a voltage of greater than 27 keV to fully fit into the loss cone, if the beam has a power of 5 kilowatt then the

gun must have a voltage of greater than 49 keV to fully fit into the loss cone, and if the beam has a power of 10 kilowatt then the gun must have a voltage of greater than 62 keV to fully fit into the loss cone.

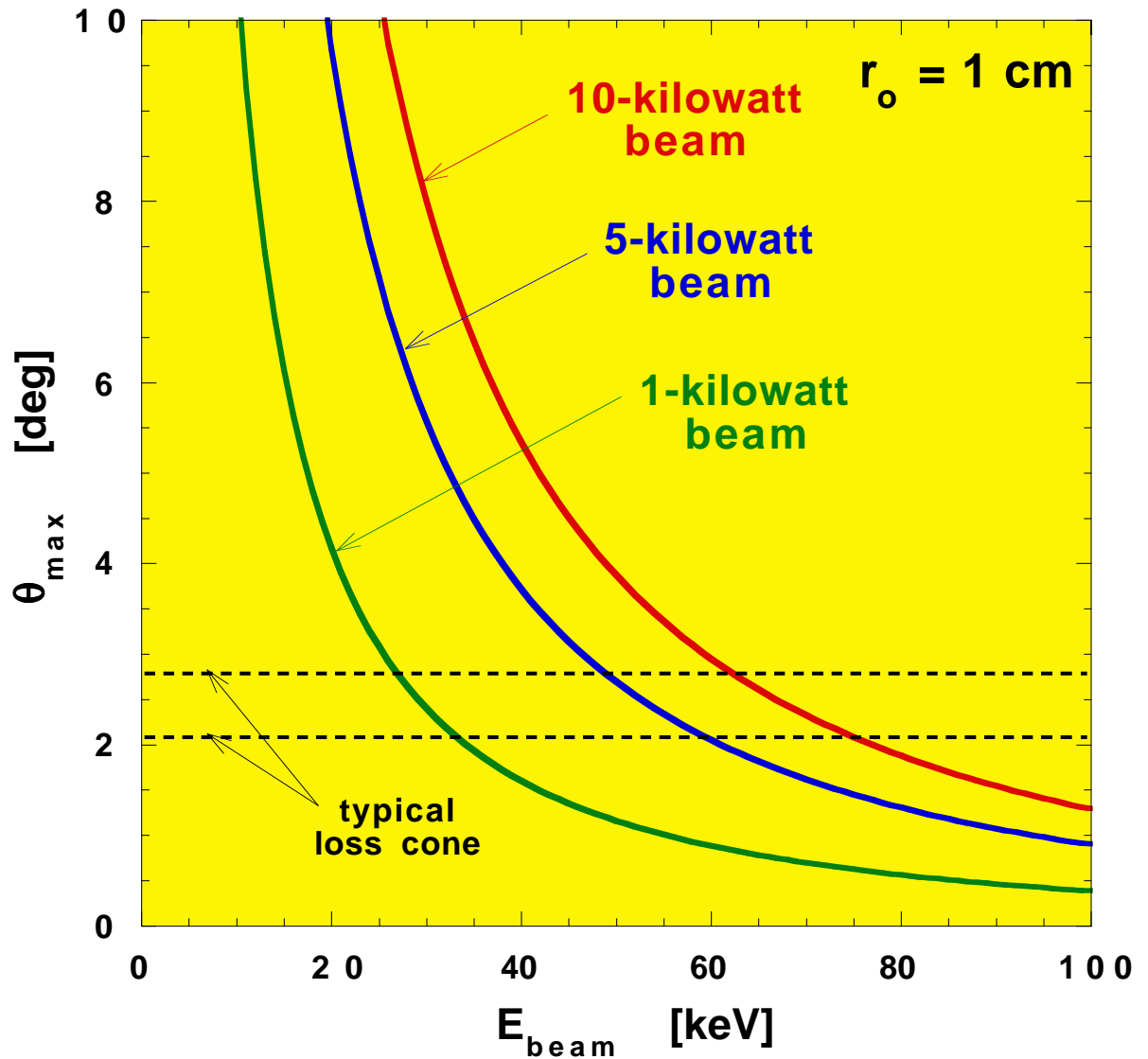


Figure B6. The divergence angle of an electron beam is plotted as a function of the beam kinetic energy for three different values of the beam power: 10 kW (red), 5 kW (blue) and 1 kW (green). A comparison is made with the typical range of values of the loss cone.

By running a large number of numerical calculations in which the beam energy \mathcal{E}_{beam} , the beam current I_{beam} , the beam initial radius r_0 , and the ambient magnetic-field strength B_0 were independently varied, as shown in Figure B7 a-d, and then fitting the results with curves, an expression for the maximum pitch angle θ_{max} of the beam as a function of those parameters can be

obtained, which is valid in the vicinity of $E_{\text{beam}} = 60 \text{ keV}$, $I_{\text{beam}} = 0.166 \text{ Amp}$, $r_o = 1 \text{ cm}$, and $B_o = 100 \text{ nT}$. That expression is

$$\theta_{\text{max}} \approx 546.5^\circ \left(\frac{E_{\text{beam}}}{1 \text{ keV}} \right)^{-0.993} \left(\frac{I_{\text{beam}}}{1 \text{ Amp}} \right)^{0.523} \left(\frac{r_o}{1 \text{ cm}} \right)^{-0.0460} \left(\frac{B_o}{1 \text{ nT}} \right)^{-0.0455} \quad (13)$$

Note that θ_{max} is relatively insensitive to the values of r_o and B_o . As expression (13) indicates, a given set of beam parameters E_{beam} , I_{beam} , and r_o corresponds to a spread θ_{max} of the beam electrons. Since $\theta_{\text{max}} \propto I_{\text{beam}}^{0.523}$, for a given beam energy E_{beam} , increasing the beam power $P_{\text{beam}} = E_{\text{beam}} I_{\text{beam}}$ by increasing I_{beam} will increase the angular spread of the beam. Too much power and the beam will not fit into the loss cone. Setting $\theta_{\text{max}} = \theta_{\text{lc}}$ in expression (13), using expression (1) for θ_{lc} with the small-angle approximation $\theta_{\text{lc}} \approx (B_o/B_{\text{atmos}})^{1/2}$ with $B_{\text{atmos}} \approx 5.5 \times 10^4 \text{ nT}$, and using $P_{\text{beam}} = E_{\text{beam}} I_{\text{beam}}$ to eliminate I_{beam} in expression (13) yields, after some manipulation and after turning degrees into radians,

$$P_{\text{beam}} \approx 3.36 \times 10^{-5} \text{ kWatt} \left(\frac{E_{\text{beam}}}{1 \text{ keV}} \right)^{2.899} \left(\frac{B_o}{1 \text{ nT}} \right)^{1.045} \left(\frac{r_o}{1 \text{ cm}} \right)^{0.0880} \quad (14)$$

for the maximum beam power that can be put into the loss cone. Since P_{beam} is such a strong function of E_{beam} , if more power is desired, higher gun voltages are desired. Note also that the initial beam radius r_o has little affect on the amount of power that can be put into the loss cone.

Scaling of the Beam Divergence Angle

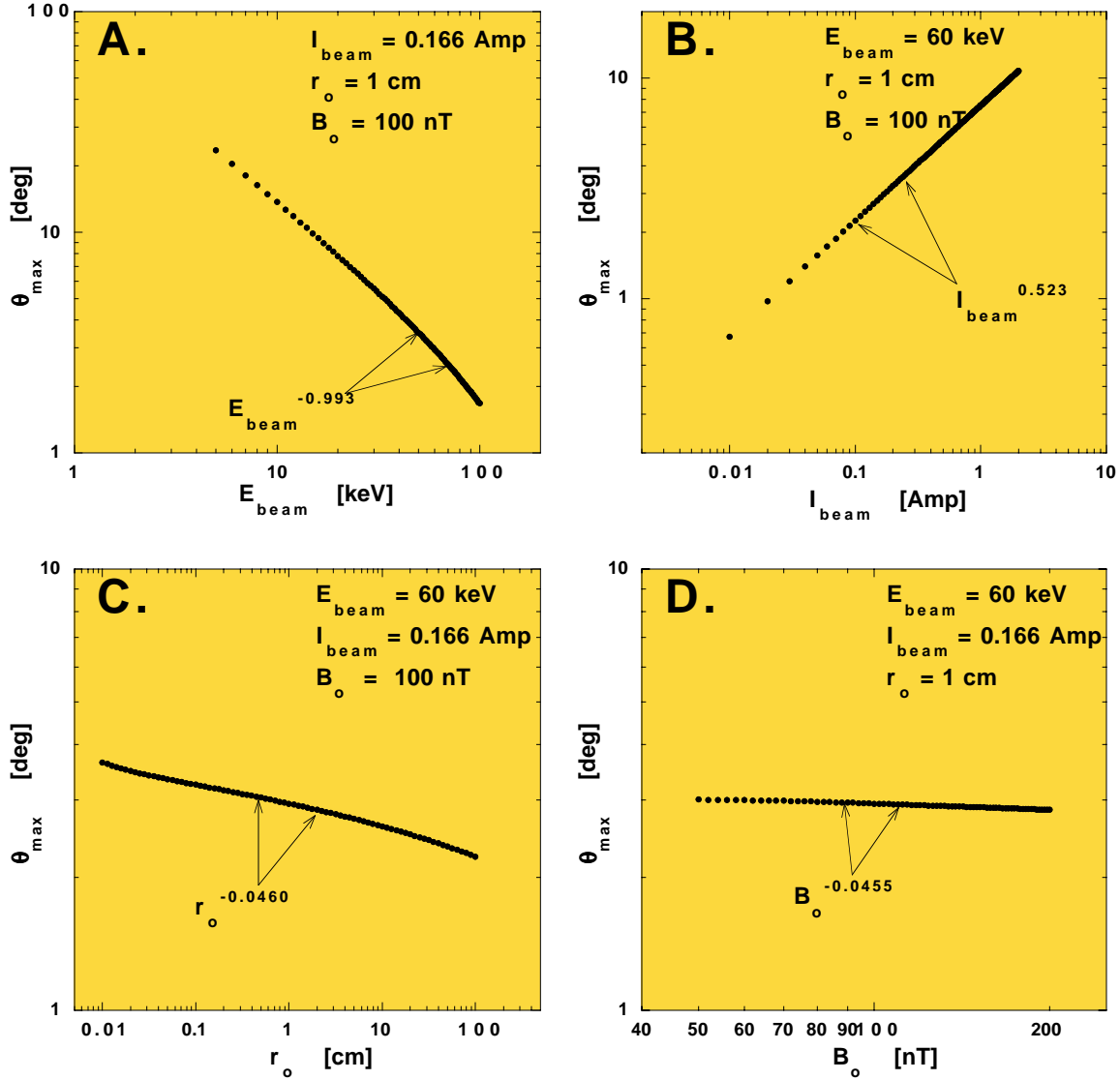


Figure B7. By varying one parameter at a time in a series of transverse-beam-dynamics calculations, the functional form of the beam divergence angle versus the beam kinetic energy (A), the beam current (B), the initial radius of the beam (C), and the ambient magnetic field (D) are determined. In each panel, power-law fits are made over the range of values denoted by the arrows.

B.4. Electrostatic Shielding by the Magnetospheric Plasma: Reduced Divergence

The electron beam emitted from the gun has a very large, negative space-charge density. Associated with this nonzero space charge of the beam, there is a radial electrostatic electric field which causes the electrons of the beam to be radially accelerated outward. However, the ambient plasma of the magnetosphere, and any plasma associated with a plasma contactor on the satellite that houses the electron gun, has free charge which can move in response to the beam electric field to shield the space charge of the beam, lessening the radial electrostatic repulsion of the beam electrons and hence lessening the beam divergence.

In the top panel of Figure B8, the density of the front the electron beam propagating into vacuum is plotted as a function of (logarithmic) time. The parameters chosen are $E_{\text{beam}} = 60 \text{ keV}$, $I_{\text{beam}} = 0.166 \text{ Amp}$, $r_0 = 1 \text{ cm}$, and $B_0 = 1 \times 10^{-3} \text{ gauss}$. As can be seen, at early times the number density of the beam is orders of magnitude greater than the density ($n_{\text{plasma}} \sim 0.5 \text{ cm}^{-3}$) that the ambient plasma would have and as the beam expands radially its density drops to well below the density that the ambient plasma would have. In vacuum, the beam oscillates radially between high density and low density.

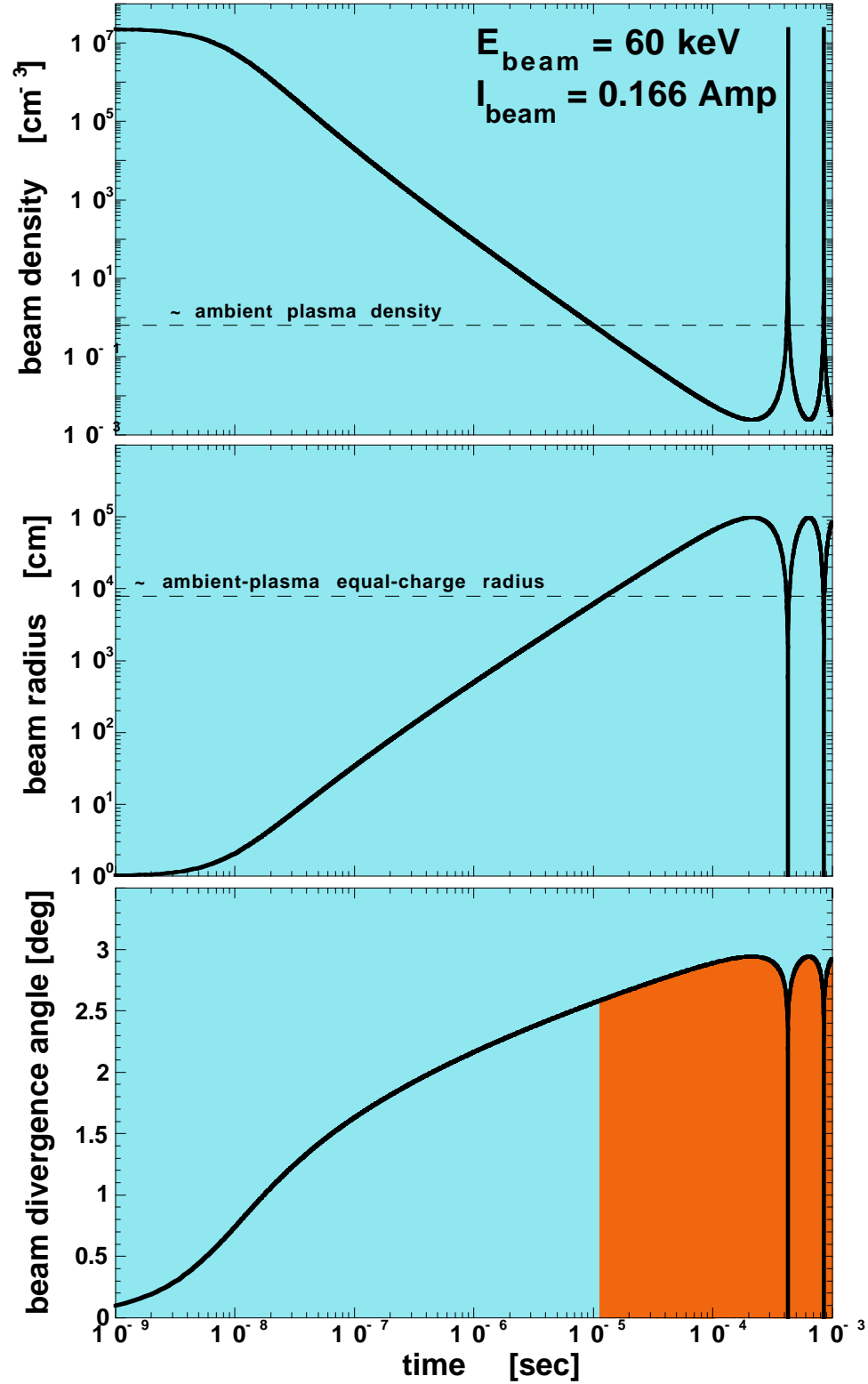


Figure B8. From a computer simulation of the transverse dynamics of the MIO electron beam the density (top panel), outer radius (middle panel), and divergence angle (bottom panel) of the beam are plotted as functions of time, with emphasis on early times after exiting the electron gun. Comparisons are made to the ambient plasma density and to the beam equal-charge radius.

The dynamic reaction of the ambient electrons and ambient ions to the beam's electric field occurs on a timescale that is, respectively, related to the electron-plasma period and ion-plasma period of the ambient plasma. The quantities that are pertinent when considering how and how fast this ambient plasma may shield the beam's space charge are the electron plasma period τ_{pe} , the electron gyroperiod τ_{ce} , the ion plasma period τ_{pi} , and the ion gyroperiod τ_{ci} . For a typical magnetospheric plasma at geosynchronous orbit, which has $n_{\text{plasma}} \sim 0.5 \text{ cm}^{-3}$, and $B \sim 100 \text{ nT}$, these pertinent numbers are $\tau_{pe} = 1.6 \times 10^{-4} \text{ sec}$, $\tau_{ce} = 3.6 \times 10^{-4} \text{ sec}$, $\tau_{pi} = 6.7 \times 10^{-3} \text{ sec}$, and $\tau_{ci} = 6.6 \times 10^{-1} \text{ sec}$. Since $\tau_{pi} \ll \tau_{ci}$ the ion response is definitely unmagnetized, and since $\tau_{pe} < \tau_{ce}$ the electron response is fairly unmagnetized. According to the study of *Borovsky* [1988], a positively charged object discharges by drawing in ambient electrons and these electrons initially discharge a cylindrical object in a time that is slightly more than $\tau_{pe}/4$. Thereafter, the electron discharge rings with a frequency (for a cylindrical object) that is slightly less than the electron plasma period τ_{pe} . A negatively charged object, such as the electron beam, is discharged when ambient ions are drawn in by the object's electric field, and these ions discharge a cylindrical object in a time that is somewhat more than $\tau_{pi}/3$. In the case of negative objects discharged by ions, the discharge does not ring, but rather the discharging is more-or-less complete in a time that is somewhat longer than $\tau_{pi}/3$.

The dynamic shielding of the beam by the ambient plasma is depicted in Figure B9, where the front 400 km of the beam is sketched. The beam is propagating to the right. As the front of the beam passes through undisturbed ambient plasma, the plasma begins to respond owing to the sudden introduction of the beam's radial electric field into the plasma. It takes a time of about $\tau_{pi}/3$ for the ions to move radially inward to shield the beam, so portions of the beam that are further than a distance $d \approx v_{\text{beam}} \tau_{pi}/3$ behind the front end of the beam are shielded by a radial inflow of the ambient ions and all radial-electric-field effects are greatly reduced. One radial-electric-field effect is the radial expansion and contraction of the beam. In Figure B9, this is depicted by the front portions of the beam undergoing radial oscillations at $\sim \tau_{ce}$ and the latter portions of the beam not undergoing these oscillations. (Note that the radial displacement, which is on the order of a km, is greatly exaggerated in the sketch.)

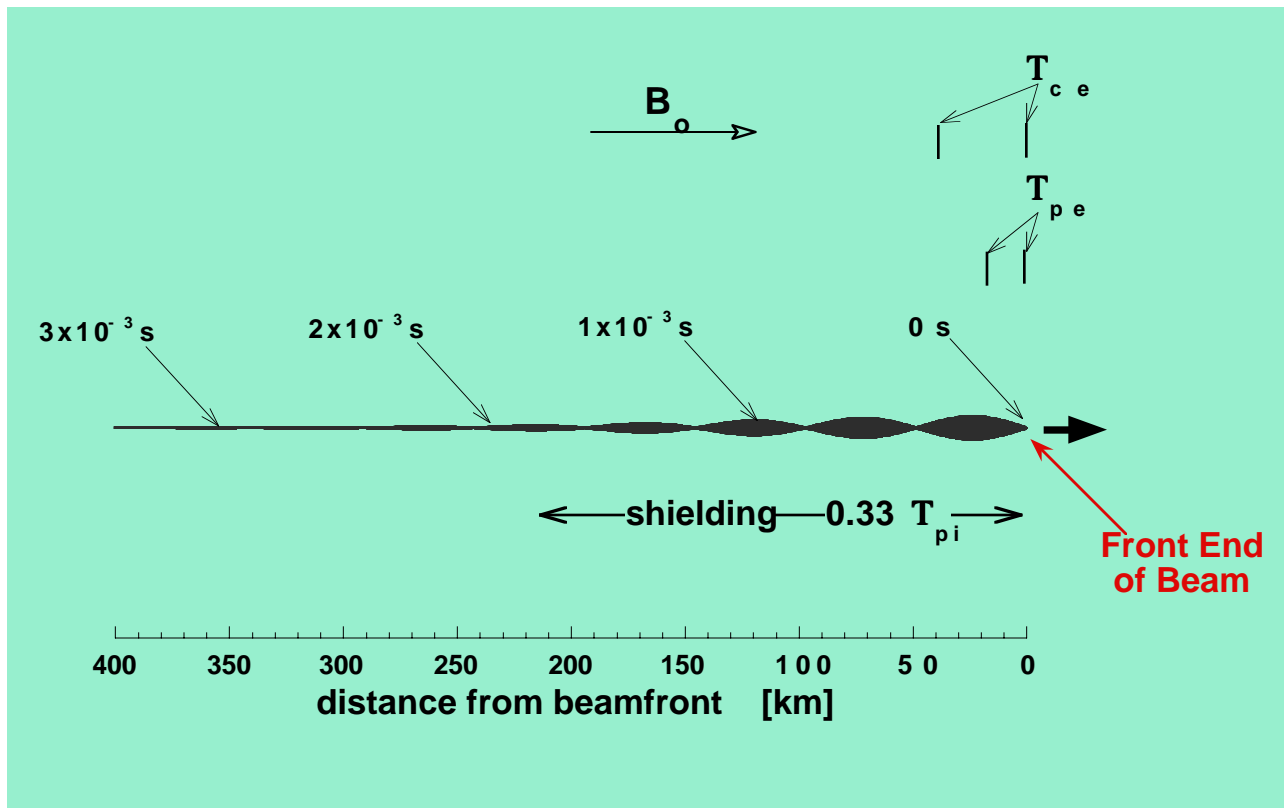


Figure B9. A sketch of the leading portion of the MIO electron beam with dynamical shielding of the beam by the radial movement of ambient magnetospheric protons onto the beam to reduce the beam's negative space charge.

One important consequence of this shielding of the space charge of the electron beam by the radial inflow of ambient ions is that the radial expansion of latter portions of the electron beam will be significantly reduced. Accordingly, the divergence angle of the latter portions of the electron beam will be much less than the divergence angle of an electron beam propagating into vacuum. This will improve the ability of the beam to fit into the loss cone. For the parameters chosen, only the first 2 milliseconds of the beam are wasted with a large divergence: the rest of the beampulse should have a small divergence angle.

At times earlier than $\tau_{pi}/3$, there will be a partial shielding of the radial electric field of the electron beam during times when the beam has expanded to a radius that is greater than the equal-charge radius r_{charge} of the beam in the plasma; this is known as ion focusing of the electron beam [e.g. *Uhm and Joyce*, 1991; *Barov and Rosenzweig*, 1994]. For this partial shielding, only a response of the ambient electrons is needed, which is rapid, not a response of the ions, which is sluggish. This shielding works as follows. As the electron beam moves into the ambient plasma, the electrons of the ambient plasma are pushed outward by the radial electric field of the electron beam,

leaving the ambient ions unshielded. If the ambient electrons move outward a sufficient distance, then the amount of unshielded ion space charge can be equal (and opposite to) the charge of the electron beam. The radial distance that the ambient electrons have to move for this to occur is out to a distance known as the equal-charge radius r_{charge} . This radius is calculated by equating the charge per unit length of the beam (which, as indicated in expression (3), is equal to $I_{\text{beam}}/v_{\text{beam}}$) with the amount of charge per unit length in the bared ions:

$$\frac{I_{\text{beam}}}{v_{\text{beam}}} = \pi n_{\text{plasma}} e r_{\text{charge}}^2 \quad (15)$$

Solving this for r_{charge} yields

$$r_{\text{charge}} = \left(\frac{I_{\text{beam}}}{v_{\text{beam}} \pi e n_{\text{plasma}}} \right)^{1/2} \quad (16)$$

For the parameters of Figure 8 ($I_{\text{beam}} = 0.166$ Amp, $v_{\text{beam}} = 1.45 \times 10^{10}$ cm/sec, and $n_{\text{plasma}} = 0.5 \text{ cm}^{-3}$), the equal charge radius is $r_{\text{charge}} = 6.8 \times 10^3$ cm, as indicated in the second panel of Figure B8. Note that the equal-charge radius is smaller than the maximum radius of the electron beam during its expansion-and-contraction cycle. During the full-expansion portions of the cycle, the positive space charge of the bare ambient ions will provide a radially inward force on the beam electrons preventing them from expanding much beyond the equal-charge radius. (This is the "ion focusing" of the beam.) However, as can be seen in the bottom panel of Figure B8 where the divergence angle of the outer portion of the beam (in vacuum) is plotted as a function of time, if the beam were to be prevented from expanding beyond the equal-charge radius then the reduction in divergence angle would not be great. Times when the radius of the beam exceeds the equal-charge radius are shaded in the bottom panel of Figure B8. For this example, the reduction in maximum divergence angle would only be from about 2.9° to about 2.5° .

B.5. Summary of Appendix B

For beam divergence, the worst-case scenario is propagation of the electron beam through a vacuum where the negative space charge of the beam is not neutralized. In that case, the maximum beam-divergence angle θ_{max} is given by expression (13). For various beam powers, this maximum divergence angle is plotted as a function of beam kinetic energy in Figure B6, where it is compared with the size of the atmospheric loss cone as seen from the geosynchronous-orbit equator.

Shielding of the space charge of the beam by the ambient plasma is a complicated process.

The radial inflow of ambient ions into the path of the electron beam, which occurs on a timescale of about τ_{pi} , which is on the order of a few milliseconds, is probably an important effect which will substantially reduce the divergence angle of the portions of the beampulse behind the front of the beam. This effect is sketched in Figure B9. The "ion focusing" of the front portions of the beam owing to a very fast radially outward displacement of the ambient electrons, which leaves the ions undisturbed but unshielded, is probably not an important effect.

B.6. Future Work

To investigate the possibility of flying an MIO electron gun that operates at lower voltage and thus save weight, a better job must be done to calculate and simulate the behavior of the beam as it propagates through an ambient magnetospheric plasma. These calculations and simulations should deal with the dynamic shielding of the beam owing to the rapid response of magnetospheric electrons and the slow response of magnetospheric ions, all in the presence of the magnetospheric magnetic field.

Appendix C: Electrostatic Two-Stream Instabilities

A naive application of an infinite-homogeneous-plasma analysis for the electrostatic two-stream instability would indicate that, after beam expansion, the electron beam from the MIO experiment would be highly unstable to the production of Langmuir waves in the magnetosphere. Should such Langmuir waves be produced, the beam would be highly scattered. However, owing to the finite radius of the expanded beam, which is comparable to the wavelength of the Langmuir waves that would be driven, the growthrate of the electrostatic two-stream instability is reduced by more than three orders of magnitude. This great reduction in growth makes the beam, in effect, stable and able to propagate through the magnetospheric plasma.

For an 60-keV 0.166-Amp electron beam (which has 10 kW of power), the beam velocity is $v_{\text{beam}} = 1.45 \times 10^{10}$ cm/sec. After 0.5 gyroperiods of propagation (which is at a time $\sim 2 \times 10^{-4}$ sec in the ~ 100 nT magnetic field at the geosynchronous equator) the beam expands (owing to its space charge) to a radius $r_{\text{beam}} \sim 9.70 \times 10^4$ cm, at which time the beam has a number density $n_{\text{beam}} \sim 2.4 \times 10^{-3}$ cm $^{-3}$.

In the nightside magnetosphere at geosynchronous orbit, a typical electron environment is $n_{\text{mag}} \sim 0.75$ cm $^{-3}$ and $T_e \sim 1.5$ keV. These magnetospheric numbers yield $\lambda_{\text{De}} = 3.3 \times 10^4$ cm for the Debye length, $\omega_{\text{pe}} = 4.02 \times 10^4$ sec $^{-1}$ for the electron-plasma frequency, and $v_{\text{Te}} = 1.63 \times 10^9$ cm/sec for the electron thermal speed.

Comparing the MIO-beam parameters with the magnetospheric-electron parameters, one finds that $n_{\text{beam}} \sim 3.2 \times 10^{-3} n_{\text{mag}}$, that $r_{\text{beam}}/\lambda_{\text{De}} \sim 2.9$, and that $v_{\text{beam}} \sim 8.9 v_{\text{Te}}$. Since $n_{\text{beam}} \ll n_{\text{mag}}$ and $v_{\text{beam}} \gg v_{\text{Te}}$, we expect the two-stream instability to have a frequency ω (in the reference frame of the magnetospheric plasma) that is $\omega \sim \omega_{\text{pe}}$ and a phase velocity ω/k that is $\omega/k \sim v_{\text{beam}}$.

If one were to use an infinite-homogeneous-plasma analysis of this beam propagating through that plasma, one would conclude that the beam drives a Langmuir wave that has a wavelength of a hundred-or-so Debye lengths that grows in a distance of several-hundred Debye lengths (it grows in 10's of electron-plasma periods). However, owing to the finite radius of the beam, the beam is not so strong a driver, and the actual growth of the two-stream instability is much slower. (The growth is nonzero, but slow.) The physical reason for this slowing of the growth is as follows. A two stream instability is a feedback between a wave in the background plasma and a

wave in the plasma of the beam. Each wave is a normal mode of that plasma (background or beam). Owing to a doppler shift associated with the velocity of the beam, the background-plasma wave and the beam wave can be the same wave. A sinusoidal wave is supported by a sinusoidal space-charge perturbation, which is a bunching of the particles of the plasma. The two-stream wave is unstable because a bunching of the particles of the plasma leads to a bunching of the particles of the beam, and a bunching of the particles of the beam leads to a bunching of the particles of the plasma, producing an unstable feedback with increased levels of bunching in the background and in the beam. The finite radius of the beam weakens this two-stream instability as follows. When particles of the beam bunch up, they produce an electric field and it is this electric field that causes the particles of the background plasma to be perturbed into a further bunching. If the wavelength of the bunching is much less than the radius of the beam, then the planar sheets of charge in the beam give rise to a robust electric field. However, if the wavelength is small compared with the radius of the beam, then the electric field of the bunched beam is weakened owing to geometrical effects (the field lines fringe out of the beam, etc.), and the ability of the bunched beam to perturb the background-plasma particles is greatly weakened, lessening the feedback and therefore slowing the instability.

Mathematically, the finite-beam-radius effects on the two-stream instability have been worked out by *Galvez and Borovsky* [1988]. Figure C.1, taken from Fig. 3 of *Galvez and Borovsky*, is relevant to the parameters of the MIO beam in the magnetosphere. The major difference is that the parameters of the figure are for a beam density that is 1/100 of the background density and the case of interest for MIO is a beam density that is 1/800 of the background density. This means that the driving in the MIO case will be even weaker than the case analyzed by *Galvez and Borovsky* (the driving goes approximately as $n_{\text{beam}}^{1/3}$, so one would expect a growthlength for MIO that is about twice as far as the growthlength obtained by *Galvez and Borovsky*). In the figure, the pertinent parameter is $r_{\text{beam}}/\lambda_{\text{De}} \sim 3.2$, which is indicated with an arrow on the horizontal axis of the graph. As can be seen, $r_{\text{beam}}/\lambda_{\text{De}} = 3.2$ the growthlength of the instability is about $3 \times 10^5 \lambda_{\text{De}}$. With $\lambda_{\text{De}} \sim 3.3 \times 10^4$ cm, this is a growthlength of about 15 R_E , implying that this instability will not be a problem for the flight of the beam through the magnetosphere.

Electrostatic Two-Stream Instability

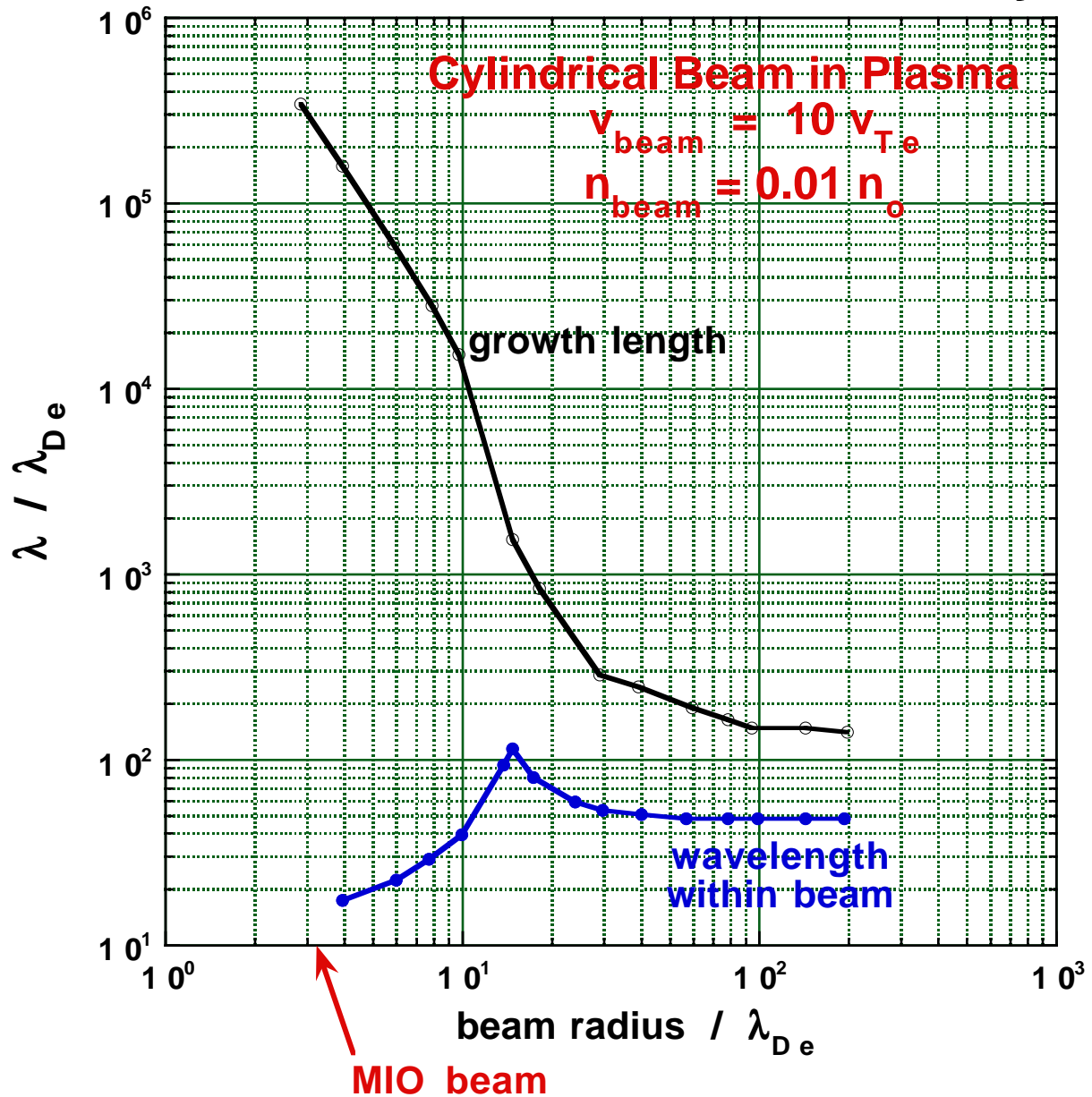


Figure C.1. The wavelength (blue) and growthlength (black) for an electrostatic plasma wave driven by a cylindrical beam. (After Figure 5 of *Galvez and Borovsky* [1988].

Note in the attached figure that the growthrate that one would obtain from an infinite-homogeneous-plasma analysis (where $r_{\text{beam}} \rightarrow \infty$) would be about $140 \lambda_{De}$, which is about 46 km. This is about 3 orders of magnitude faster growth than the finite-beam-radius analysis yields.

References

- Ahlen, S. P. Theoretical and experimental aspects of the energy loss of relativistic heavily ionizing particles, *Rev. Mod. Phys.*, 52, 121, 1980.
- Alfven, H., and C.-G. Fälthammar, *Cosmical Electrodynamics*, sects. 2.2.1 and 2.3.6, Oxford University Press, New York, 1963.
- Banks, P. M., C. R. Chappell, and A. F. Nagy, A new model for the interaction of auroral electrons with the atmosphere: Spectral degradation, backscatter, optical emission, and ionization, *J. Geophys. Res.*, 79, 1459, 1974.
- Barov, N., and J. B. Rosenzweig, Propagation of short electron pulses in underdense plasmas, *Phys. Rev. B*, 49, 4407, 1994.
- Boehm, M. H., J. Clemmons, J.-E. Wahlund, A. Eriksson, L. Eliasson, L. Blomberg, P. Kintner, and H. Hofner, Observations of an upward-directed electron beam with the perpendicular temperature of the cold ionosphere, *Geophys. Res. Lett.*, 22, 2103, 1995.
- Borovsky, J. E., The dynamic sheath: Objects coupling to plasmas on electron-plasma-frequency time scales, *Phys. Fluids*, 31, 1074, 1988.
- Borovsky, J. E., Auroral arc thicknesses as predicted by various theories, *J. Geophys. Res.*, 98, 6101, 1993.
- Borovsky, J. E., D. M. Suszcynsky, M. I. Buchwald, and H. V. DeHaven, Measuring the Thickness of Auroral Curtains, *Arctic*, 44, 231, 1991.
- Borovsky, J. E., D. J. McComas, M. F. Thomsen, J. L. Burch, J. Cravens, C. J. Pollock, T. E. Moore, and S. B. Mende, Magnetosphere-Ionosphere Observatory (MIO): A multisatellite mission designed to solve the problem of what generates auroral arcs, *Eos Trans. Amer. Geophys. Union.*, 79(45), F744, 2000.
- Borovsky, J. E., R. A. Greenwald, T. J. Hallinan, J. L. Horwitz, M. C. Kelley, D. M. Klumpar, R. L. Lysak, B. H. Mauk, T. E. Moore, G. D. Reeves, H. J. Singer, and M. F. Thomsen, The Magnetosphere-Ionosphere Facility: A satellite cluster in geosynchronous orbit connected to ground-based observatories, *Eos Trans. Amer. Geophys. Union*, 81(19), S398, 1998.
- Dalgarno, A., I. D. Latimer, and J. W. McConkey, Corpuscular bombardment and N_2^+ radiation, *Planet. Space Sci.*, 13, 1008, 1965.
- Davis, T. N., W. N. Hess, M. C. Trichel, E. M. Wescott, T. J. Hallinan, H. C. Stenbaek-Nielsen, and E. J. R. Maier, Artificial aurora conjugate to a rocket-borne electron accelerator, *J. Geophys. Res.*, 85, 1722, 1980.
- Elphinstone, R. D., D. Hearn, J. S. Murphree, and L. L. Cogger, Mapping using the Tsyganenko Long magnetospheric model and its relationship to Viking auroral images, *J. Geophys. Res.*, 96, 1467, 1991.
- Fairfield, D. H., and K. Takahashi, *1983 Tail-Era Data Series Vol. 4: GOES 5 and GOES 6 Geosynchronous Magnetic Field Data*, NASA National Space Science Data Center Report 91-07, March, 1991.
- Fink, M., and J. Ingram, Theoretical electron scattering amplitudes and spin polarizations, *Atomic*

Data, 4, 129, 1972.

Galvez, M., and J. E. Borovsky, The electrostatic two-stream instability driven by slab-shaped and cylindrical beams injected into plasmas, *Phys. Fluids*, 31, 857, 1988.

Goldstein, H., *Classical Mechanics*, Second Edition, sect. 7.6, Addison-Wesley, Reading, Massachusetts, 1981.

Green, A. E. S., and C. A. Barth, Calculations of ultraviolet molecular nitrogen emissions from the aurora, *J. Geophys. Res.*, 70, 1083, 1965.

Hallinan, T. J., J. Winkler, P. Malcolm, H. C. Stanbaek-Nielsen, and J. Baldrige, Conjugate echoes of artificially injected electron beams detected optically by means of new image processing, *J. Geophys. Res.*, 95, 6519, 1990.

Hedin, A. E. 1987. MSIS-86 thermospheric model, *J. Geophys. Res.*, 92, 4649, 1987.

Hones, E. W., M. F. Thomsen, G. D. Reeves, L. A. Weiss, D. J. McComas, and P. T. Newell, Observational determination of magnetic connectivity of the ggg region of the magnetosphere to the auroral oval, *J. Geophys. Res.*, 101, 2629, 1996.

ITT (International Telephone and Telegraph Corporation), *Reference Data for Radio Engineers*, sect. 28, fig. 32, Howard Sams and Co., Indianapolis, Ind., 1977.

Izhovkina, N. I., J. C. Kosik, A. K. Pyatsi, H. Reme, A. Saint-Marc, J. L. Sverdllov, M. V. Uspensky, J. M. Vigo, J. F. Zarnitsky, and I. A. Zhulin, Comparison between experimental and theoretical conjugate points locations in the Araks experiments, *Ann. Geophys.*, 36, 319, 1980.

Jursa, A. S. (ed.), *Handbook of Geophysics and the Space Environment*, Air Force Geophysics Laboratory, 1985.

Katz, I., J. N. Barfield, J. L. Burch, J. A. Marshall, W. C. Gibson, T. Neubert, W. T. Roberts, W. W. L. Taylor, and J. R. Beattie, Interactions between the space experiments with particle accelerators, plasma contactor, and the ionosphere, *J. Spacecraft Rockets*, 31, 1079, 1994.

Kremser, G., A. Korth, S. L. Ullaland, S. Perraut, A. Roux, A. Pedersen, R. Schmidt, and P. Tanskanen, Field-aligned beams of energetic electrons ($16 \text{ keV} < E < 80 \text{ keV}$) observed at geosynchronous orbit at substorm onset, *J. Geophys. Res.*, 93, 14453, 1988.

Lavergnat, J., The French-Soviet experiment ARAKS: Main results, in *Artificial Particle Beams in Space Plasma Studies*, B. Grandal (ed.), pg. 87, Plenum, New York, 1982.

Lu, G., M. Brittnacher, G. Parks, and D. Lummerzheim, On the magnetospheric source regions of substorm-related field-aligned currents and auroral precipitation, *J. Geophys. Res.*, 105, 18483, 2000.

Mauk, B. H., and C.-I. Meng, The aurora and middle magnetospheric processes, in *Auroral Physics*, edited by C.-I. Meng, M. J. Rycroft, and L. A. Frank, Pg. 223, Cambridge Press, Cambridge, 1991.

Marmier, P. and E. Sheldon, *Physics of Nuclei and Particles: Volume I*, Academic Press, New York, 1969.

McIlwain, C. E., Auroral electron beams near the magnetic equator, in *Physics of the Hot Plasma in the Magnetosphere*, edited by B. Hultqvist and L. Stenflo, Pg. 91, Plenum, New York, 1975.

Meng, C.-I., B. Mauk, and C. E. McIlwain, Electron precipitation of evening diffuse aurora and its

conjugate electron fluxes near the magnetospheric equator, *J. Geophys. Res.*, **84**, 2545, 1979.

Miller, R. B., *An Introduction to the Physics of Intense Charged Particle Beams*, secs. 3.1, 4.4.1, and 4.4.2, Plenum, New York, 1982.

Omholt, A., *The Optical Aurora*, Table 4.4 and sect. 1.1.2., Springer-Verlag, New York, 1971.

O'Neil, R. R., O. Shepherd, W. P. Reidy, J. W. Carpenter, T. N. Davis, D. Newell, J. C. Ulwick, and A. T. Stair, Excede 2 test, an artificial auroral experiment: Ground-based optical measurements, *J. Geophys. Res.*, **83**, 3281, 1978.

Pellat, R., and R. Z., Sagdeev, Concluding remarks on the ARAKS experiments, *Ann. Geophys.*, **36**, 443, 1980.

Penndorf, R., Tables of the refractive index for standard air and the Rayleigh scattering coefficient for the spectral region between 0.2 and 20.0 μ and their application to atmospheric optics, *J. Optical Soc. Amer.*, **47**, 176, 1957.

Photometrics, *Charge-Coupled Devices for Quantitative Electronic Imaging*, Photometrics, Tucson, 1990.

Prech, L., Z. Nemecek, J. Safrankova, J. Simunek, V. Truhlik, and N. M. Shutte, Response of the electron energy distribution to an artificially emitted electron beam: APEX experiment, *Adv. Space Res.*, **15**(12), 33, 1995.

Prueitt, M. L., The Excitation Temperature of Lightning, *J. Geophys. Res.*, **68**, 803, 1963.

Rapport, S. A., R. J. Rieder, W. P. Reidy, R. L. McNutt, J. J. Atkinson, and D. E. Paulsen, *J. Geophys. Res.*, **98**, 19093, 1993.

Riley, M. E., C. J. MacCallum, and F. Biggs, Theoretical electron-atom elastic scattering cross sections, *Atomic Data and Nucl. Data Tab.*, **15**, 443, 1975.

Shum, S., J. E. Borovsky, D. M. Suszcynsky, G. D. Reeves, and T. J. Hallinan, Looking into the causes of aurora: Equatorial-magnetospheric plasma measurements coordinated with simultaneous all-sky-camera observations, *Eos Trans. Amer. Geophys. Union*, **81**(XX), XXXX, 2000.

Stewart, D. T., Electron excitation functions of the first negative bands of N_2^+ , *Proc. Phys. Soc. A*, **69**, 437, 1958.

Suszcynsky, D. M., J. E. Borovsky, M. F. Thomsen, and T. J. Hallinan, Observations of the aurora near the edge of the plasmasphere: Structure in the electron plasma sheet, *Eos Trans. Amer. Geophys. Union*, **79**(17), 1998.

Tsyganenko, N. A., A magnetospheric magnetic field model with a warped tail current sheet, *Planet. Space Sci.*, **37**, 5, 1989.

Uhm, H. S., and G. Joyce, Theory of wake-field effects of a relativistic electron beam propagating in a plasma, *Phys. Fluids B*, **3**, 1587, 1991.

Uspensky, M. V., E. E. Timopheev, and Y. L. Sverdlov, "ARAKS" doppler radar measurements of the ionospheric effects of artificial electron beams in the North hemisphere, *Ann. Geophys.*, **36**, 303, 1980.

Weiss, L. A., M. F. Thomsen, G. D. Reeves, and D. J. McComas, An examination of the Tsyganenko (T89A) field model using a database of two-satellite magnetic conjunctions, *J.*

Geophys. Res., 102, 4911, 1997.

Winckler, J. R., Controlled experiments in the Earth's magnetosphere with artificial electron beams, *Rev. Mod. Phys.*, 64, 859, 1992.

Winckler, J. R., R. L. Arnoldy, and R. A. Hendrickson, Echo-2: Study of electron beams injected into the high latitude ionosphere from a large sounding rocket, *J. Geophys. Res.*, 80, 2083, 1975.

Zhulin, I. A., A. V. Kustov, M. V. Uspensky, and T. V. Miroshnikova, Radar observations of the overdense ionospheric ionization created by the artificial electron beam in the "Zarnitza-2" experiment, *Ann. Geophys.*, 36, 313, 1980.